Electronic Supplementary Material (ESI) for Journal of Materials Chemistry C.
This journal is © The Royal Society of Chemistry 2024

Supporting Information

SONOCRYSTALLIZATION INDUCED THERMALLY ACTIVATED DELAYED FLUORESCENCE VIA DISTORTION OF MOLECULAR GEOMETRY

Antonio Maggiore*[a,b], Yangyang Qu[a], Piotr Pander[c,d], Fernando B. Dias[e] , Gilles Clavier[a], Regis Guillot[f], Davide Altamura[g], Cinzia Giannini[g], Vincenzo Maiorano[b], Pierre Audebert[a] and Fabien Miomandre[a]

---

[a] Université Paris-Saclay, ENS Paris-Saclay, CNRS, PPSM, 91190, Gif-sur-Yvette, France.

[b] CNR-NANOTEC – Institute of Nanotechnology, c/o Campus Ecoteckne, Via Monteroni, 73100 Lecce, Italy

[c] Faculty of Chemistry, Silesian University of Technology, Strzody 9, 44-100 Gliwice, Poland

[d] Centre for Organic and Nanohybrid Electronics, Silesian University of Technology, Konarskiego 22B, 44-100 Gliwice, Poland

[e] Department of Physics, University of Durham, South Road, Durham, DH1 3LE, United Kingdom

[f] Université Paris-Saclay, CNRS, Institut de chimie moléculaire et des matériaux d'Orsay, 91405, Orsay, France.

[g] Institute of Crystallography CNR-IC Via Amendola 122/O, Bari 70126, Italy

Table of contents

1 MATERIALS AND METHODS

1.1 FILM FABRICATION

a) Doped PMMA films

All blends were obtained by drop-casting DCM solutions (0.05 g/L) of the compounds at room temperature on quartz slides followed by slow evaporation in solvent saturated conditions overnight. Concentration of the fluorophore in the film is reported in weight percentage (w/w) relative to the polymer mass in the solution. All blends formed clear, glassy, transparent solid films.

b) Neat films casting

The films were obtained by drop-casting DCM solutions at room temperature followed by fast (1-3 minutes) evaporation at solvent saturated conditions. The compound **Pht-BzN** forms amorphous solid film which becomes polycrystalline after 1h.

c) polycrystalline powders

As synthesized powders were collected from PE/DCM solution and studied in a 1 mm quartz cuvette.

1.2 NANOPARTICLES AND MICROCRYSTALS OBTAINED FROM THF/WATER MIXTURE AND SONICATION

After having prepared a solution of **Pht-BzN** and **Phx-BzN** in THF (1 mg/ml), 50 microliters of this solution was taken with a micropipette and added to a vial containing 3.5 ml of water. Since water is a non-solvent, the molecules aggregate to form a colloid. In order to induce crystallization of the **Pht-BzN** dispersion, we have performed sonication in an ultrasonic bath. In fact, it has already been reported in the literature that ultrasounds can be used to induce crystallization in a solution. This often finds interesting applications, *e.g.* in pharmacology and fine chemicals sectors [1-2]. Ultrasonic waves decrease the induction time and increase the nucleation rate, thanks to the intense micro-scale mixing and turbulence caused by acoustic cavitation[3] [4-7].

1.3 DLS ANALYSIS

The microcrystal dimensions obtained through sonication, was measured trough the DLS analysis techniques, by using the NanoQ Vasco 2.5.9.0 - Cordouan Technologies instrument. Dynamic Light Scattering (DLS) is a technique to characterize dilute and transparent dispersions of particles. Based on the analysis of scattered light fluctuations caused by the Brownian motion of particles, it provides sizes measurements from the nanometre scale and up to a few microns. The sizes of the microcrystals obtained in this work are around 250 and 650 nm (**Fig. S35**).

1.4 PHOTOPHYSICS

Absorption spectra were collected using a Cary 4000 double beam spectrophotometer (Agilent). Luminescence spectra were collected with a FluoroLog3 spectrofluorimeter (Horiba Jobin Yvon). The relative photoluminescence quantum yields (PLQY) in solution were determined from corrected emission spectra using quinine dication (Φ_{PL}= 0.59 in $HClO_4$[8]) as standard.

PLQYs of the films were measured by an absolute method with a barium sulphate-coated integrating sphere F-3018(Horiba) inserted into the spectrofluorimeter sample compartment.

Prompt and Delayed Fluorescence (PF and DF) and phosphorescence spectra and decays in solid state (PMMA, neat film, polycrystalline powder) were recorded by nanosecond gated luminescence and lifetime measurements (from 400 ps to 1 s) using either third harmonics of a high-energy, pulsed Nd:YAG laser emitting at 355 nm (EKSPLA) or a N_2 laser emitting at 337 nm. Emission was focused onto a spectrograph and detected on a sensitive gated iCCD camera (Stanford Computer Optics) of sub-nanosecond resolution. Using the iCCD camera and spectrograph allows individual spectra to be captured at specific time delays (TD), with given integration times (IT) after pulsed laser excitation. This technique enables simultaneous construction of decay curves with associated spectra data by collecting several spectra with logarithmically increasing TD and IT. The data were collected under vacuum at RT and under a stream of nitrogen at 80K.

The ns fluorescence decay curves in solution, were obtained by the time-correlated single-photon counting (TCSPC) method with a femtosecond laser excitation composed of a Titanium Sapphire laser (Tsunami, Spectra-Physics) pumped by a doubled Nd:YVO_4 laser (Millennia Xs, Spectra-Physics). The fluorescence data were analyzed using the Globals software package developed at the Laboratory for Fluorescence Dynamics at the University of Illinois at Urbana-Champaign, which includes deconvolution analysis and global non-linear least-squares minimization method. The quality of the fit was estimated by visual inspection of the weighted residuals and calculation of χ^2

The μs fluorescence decay curves in solution were obtained using an Edinburgh instrument LP920 laser flash photolysis spectrometer combined with an Nd:YAG laser (Continuum) tripled at 355 nm via non-linear crystals. The Levenberg Marquardt algorithm was used for non-linear least square fit (tail fit) as implemented in the L900 software (Edinburgh instrument). The quality of the fit was estimated by visual inspection of the weighted residuals and calculation of χ^2.

To calculate average lifetimes (τ_{av}) for multi-exponential fits, we used the fitting parameters such as A_i and τ_i, where A_i is amplitude of i^{th} lifetime component and τ_i is the respective lifetime value. In the decay profiles acquired using time-resolved emission measurements, the y-axis is actually the number of photons and the x-axis is arrival time. Therefore, A_i itself is not the number of photons with lifetime τ_i. This number can be obtained by calculating the area under the decay trace: $A_i \times \tau_i$.

Therefore, the average lifetime is equal to:

$$\tau_{av} = \frac{\sum A_i \tau_i^2}{\sum A_i \tau_i}$$

The rate constant k_{ISC} and k_{RISC} are determined by using the following equations[9] which are valid for a reverse intersystem crossing yield close to 100%, that occurs only if the ratio between the DF and PF (Φ_{DF}/Φ_{PF}) is around or above four[10] (DF/PF ≥ 4).

for K_{RISC}:

$$k_{RISC} = \frac{1}{\tau_{DF}}\left(1 + \frac{DF}{PF}\right)$$

Where the integrals correspond to the DF and PF regions in the decay time and τ_{DF} is the lifetime of the DF component.

And for K_{ISC}:

$$\Phi_{ISC} = \frac{\Phi_{DF}/\Phi_{PF}}{(1 + \Phi_{DF}/\Phi_{PF})} = \frac{DF/PF}{1 + DF/PF}$$

$$k_{ISC} = \frac{\Phi_{ISC}}{\tau_{PF}} = \frac{1}{\tau_{DF}}\left(\frac{DF/PF}{1 + DF/PF}\right)$$

Where DF/PF is obtained as a ratio of integrated delayed fluorescence (DF) and prompt fluorescence (PF) intensity from the fitted decay curves, while τ_{PF} is the prompt fluorescence lifetime.

2 SYNTHESIS

Cz-BzN

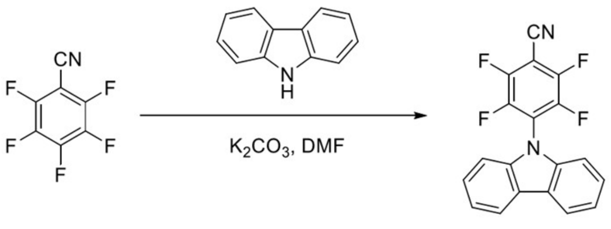

Cz-BzN

To a 50 mL two-neck round bottom flask equipped with a stir bar, carbazole (0.167 g, 1 mmol), potassium carbonate (K_2CO_3) (0.166 g, 1.2 mmol) and 6 mL of dry DMF were added under inert atmosphere. Then of 2,3,4,5,6-pentafluorobenzonitrile (PFBN, 0.125 mL, 1 mmol) was added at 0 °C and the reaction mixture was allowed to stir at room temperature overnight. After the reaction mixture was neutralized with acidified water, extracted with dichloromethane, and dried over anhydrous magnesium sulfate ($MgSO_4$).

The product first was purified by recrystallization from CH_2Cl_2 to afford 0.192 g white crystals of **Cz-BzN**. The residue was purified using silica gel chromatography (Petroleum ether: CH_2Cl_2=3:1 v/v) to yield additional 0.08 g of **Cz-BzN** as a white solid (total yield: 82%).

^{1}H NMR (400 MHz, $CDCl_3$, δ): 8.1 (dd, J = 7.8 Hz, J = 1.4 Hz, 2H), 7.5 (ddd, J = 8.2 Hz, J = 7.3 Hz, J = 1.4 Hz, 2H), 7.4 (ddd, J = 7.8 Hz, J = 7.3 Hz, J = 0.9 Hz, 2H), 7.1 (d, J = 8.2 Hz, 2H) ppm; ^{13}C NMR (100 MHz, $CDCl_3$, δ): 148.1 (dd, $^1J_{CF}$ = 264.1 Hz, $^2J_{CF}$ = 14.4 Hz), 143.7 (dd, $^1J_{CF}$ = 258.8 Hz, $^2J_{CF}$ = 12.5 Hz), 139.1, 126.9, 124.6, 122.9 (t, $^2J_{CF}$ = 14.4 Hz), 122.2, 120.8, 110.0, 107.2 (t, $^3J_{CF}$ = 4.79 Hz), 93.6 (t, $^2J_{CF}$ = 17.3 Hz) ppm; ^{19}F NMR (376 MHz, $CDCl_3$, δ): -130.5 (s, 2F), -138.1 (s, 2F) ppm;

HRMS [M]+: m/z calculated for $[C_{19}H_8N_2F_4]^+$ 340.0642, found 340.0614.

Pht-BzN

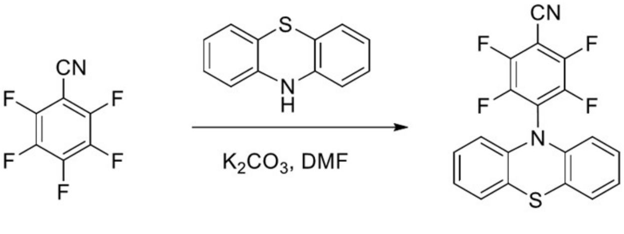

Pht-BzN

To a 50 mL two-neck round bottom flask equipped with a stir bar, phenothiazine (0.199 g, 1 mmol), potassium carbonate (K_2CO_3) (0.166 g, 1.2 mmol) and 6 mL of dry DMF were added under inert atmosphere. Then 2,3,4,5,6-pentafluorobenzonitrile (PFBN, 0.125 mL, 1 mmol) was added at 0°C and the reaction mixture was allowed to stir at room temperature overnight. After the reaction, mixture was neutralized with acidified water, extracted with dichloromethane, and dried over anhydrous magnesium sulfate ($MgSO_4$). The product was purified using silica gel chromatography (Petroleum ether:CH_2Cl_2= 3:1 v/v) to give 0.298 g of **Pht-BzN** as a pale yellow solid (yield: 80%). Single crystals of **Pht-BzN** were grown by slow evaporation from petroleum ether/dichloromethane (3:1) mixture.

^{1}H NMR (400 MHz, $CDCl_3$, δ): 7.1-7.1 (m, 2H), 7.0 -6.9 (m, 4H), 6.3 (dd, J = 7.8 Hz, J = 1.4 Hz, 2H) ppm; ^{13}C NMR (100 MHz, $CDCl_3$, δ): 148.3 (dd, $^1J_{CF}$ = 265.5 Hz, $^2J_{CF}$ = 15.3 Hz), 146.5 (dd, $^1J_{CF}$ = 258.8 Hz, $^2J_{CF}$ = 13.4 Hz), 141.0, 127.6, 127.5, 126.9 (t, $^2J_{CF}$ = 15.3 Hz), 124.7, 123.1, 115.7, 107.1 (t, $^3J_{CF}$ = 4.8 Hz), 95.4 (t, $^2J_{CF}$ = 17.3 Hz) ppm; ^{19}F NMR (376 MHz, $CDCl_3$, δ): -130.0 (s, 2F), -138.2 (s, 2F) ppm;

HRMS [M]+: m/z calculated for $[C_{19}H_8N_2SF_4]^+$ 372.0344, found 372.0345.

3 SUPPLEMENTARY DATA

3.1 X-RAY DIFFRACTION ANALYSIS (XRD)

X-ray diffraction data for compounds **Cz-BzN**, **Phz-BzN** & **Pht-BzN** were collected by using a Kappa X8 APPEX II Bruker diffractometer with graphite-monochromated $Mo_{K\alpha}$ radiation (λ = 0.71073 Å).

The **Phx-BzN** structure has already been published previously[11].

Crystals were mounted on a CryoLoop (Hampton Research) with Paratone-N (Hampton Research) as cryoprotectant and then flashfrozen in a nitrogen-gas stream at 100 K. For compounds, the temperature of the crystal was maintained at the selected value by means of a 700 series Cryostream cooling device to within an accuracy of ±1K. The data were corrected for Lorentz polarization, and absorption effects. The structures were solved by direct methods using SHELXS-97[12] and refined against *F*[13] by full-matrix least-squares techniques using SHELXL-2018[2] with anisotropic displacement parameters for all non-hydrogen atoms. Hydrogen atoms were located on a difference Fourier map and introduced into the calculations as a riding model with isotropic thermal parameters. All calculations were performed by using the Crystal Structure crystallographic software package WINGX[14]. The crystal data collection and refinement parameters are given in **Table S1**. CCDC 2084889 & 2243330-2243331 contain the supplementary crystallographic data for this paper. These data can be obtained free of charge from the Cambridge Crystallographic Data Centre via http://www.ccdc.cam.ac.uk/Community/.

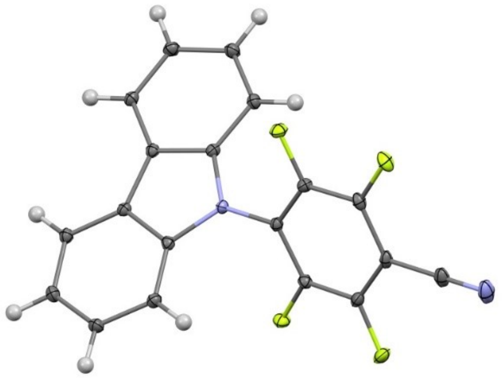

Figure S1: *An ORTEP drawing of compound* ***Cz-BzN.*** *Thermal ellipsoids are shown at the 30% probability level.*

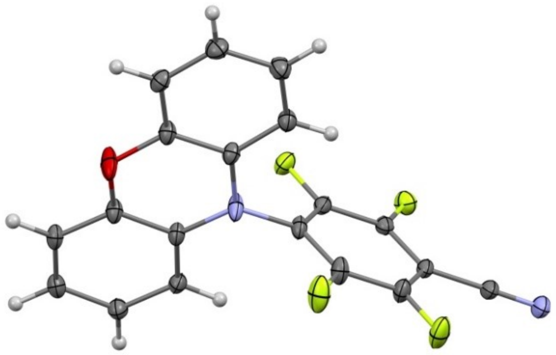

Figure S2: *An ORTEP drawing of compound* ***Phx-BzN****. Thermal ellipsoids are shown at the 30% probability level.*

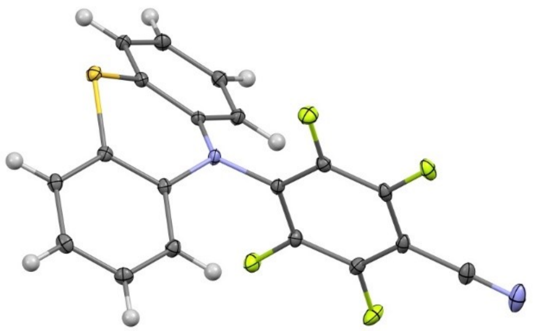

Figure S3: *An ORTEP drawing of compound* ***Pht-BzN****. Thermal ellipsoids are shown at the 30% probability level. For the sake of clarity, only one molecule of the asymmetric unit is shown.*

Table S1. Crystallographic data and structure refinement details.

Compound	**Cz-BzN**	**Phx-BzN**	**Pht-BzN**
CCDC	2243330	2084889	2243331
Empirical Formula	$C_{19}\ H_8\ F_4\ N_2$	$C_{19}\ H_8\ F_4\ N_2\ O$	$C_{19}\ H_8\ F_4\ N_2\ S$
M_r	340.27	356.27	372.33
Crystal size, mm^3	0.31 x 0.08 x 0.04	0.29 x 0.26 x 0.13	0.31 x 0.28 x 0.12
Crystal system	orthorhombic	monoclinic	triclinic
Space group	$P\ b\ c\ n$	$P\ 2_1/c$	P -1
a, Å	7.1863(3)	15.3603(3)	7.5813(2)
b, Å	12.9975(5)	6.60040(10)	12.9249(3)
c, Å	15.4834(8)	15.1377(3)	17.5802(4)
α, °	90	90	109.8140(10)

β, °	90	96.5630(10)	97.8320(10)
γ, °	90	90	98.0790(10)
Cell volume, Å^3	1446.21(11)	1524.67(5)	1572.99(7)
Z ; Z’	4 ; 1/2	4 ; 1	4 ; 2
T, K	100(1)	100(1)	100(1)
Radiation type ; wavelength Å	MoKα ; 0.71073	MoKα ; 0.71073	MoKα ; 0.71073
F_{000}	688	720	752
μ, mm^{-1}	0.130	0.131	0.254
range, °	2.631 - 30.556	2.670 - 30.686	1.256 - 30.634
Reflection collected	9 978	33 453	34 065
Reflections unique	2 209	4 698	9 425
R_{int}	0.0394	0.0299	0.0271
GOF	1.042	1.039	1.030
Refl. obs. (*I*>2(*I*))	1 521	3 558	7 742
Parameters	116	235	469
wR_2 (all data)	0.1218	0.1156	0.0923
R value (*I*>2(*I*))	0.0436	0.0417	0.0347
Largest diff. peak and hole (e-.Å^{-3})	0.352 ; -0.314	0.355 ; -0.210	0.402 ; -0.311

Table S2: Main angles for the XRD structures of **Cz-BzN**, **Phx-BzN**, **Pht-BzN**.

	D (°)[a]	**D-A (°)**[b]	**D-A (°)** **dihedral angle**
Cz-BzN	2.71	50.14	50.70
Phz-BzN	4.90	78.17	83.31
Pht-BzN	42.68 (mol1), 33.75 (mol2)	79.58 (mol1), 81.19 (mol2)	89.22 (mol1), 86.11 (mol2)

a) D angle refers to the angle between the mean planes of the two phenyl rings of the Donor; b) A-D angle refers to the angle between the mean planes of the Donor and the Acceptor.

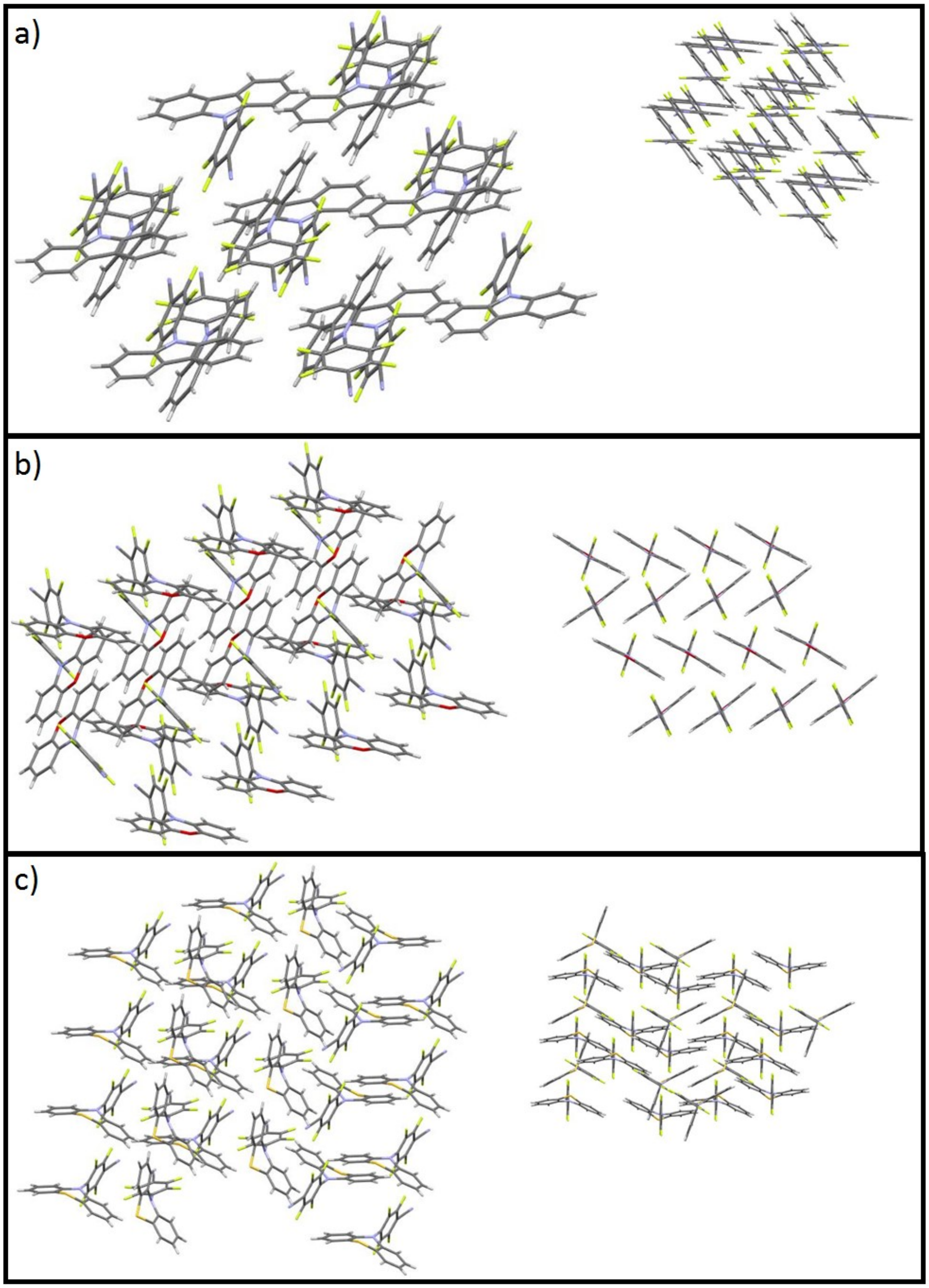

Figure S4:* *a) *Molecular packing in **Cz-BzN** crystal;* **b)** *molecular packing in **Phx-BzN** crystal;* ***c)*** *molecular packing in **Pht-BzN** crystal**.***

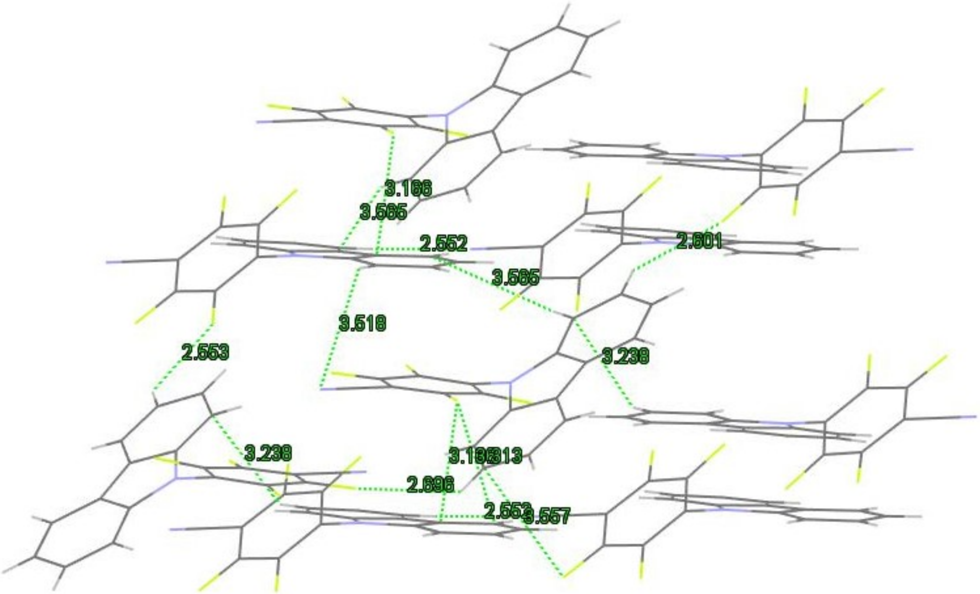

Figure S5: Molecular packing with intermolecular interactions in crystal ***Cz-BzN****.*

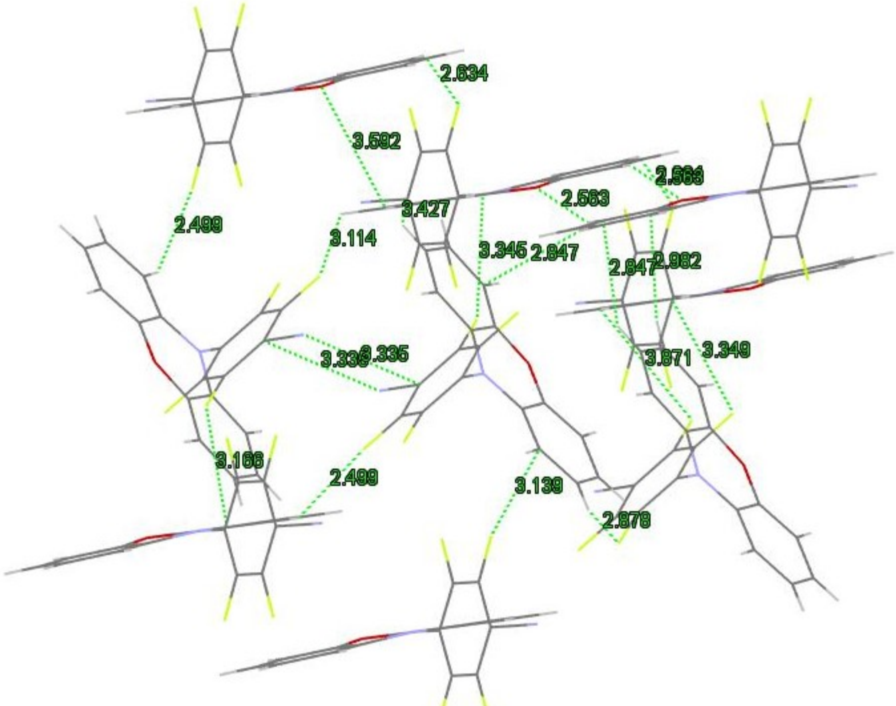

Figure S6: Molecular packing with intermolecular interactions in crystal ***Phx-BzN****.*

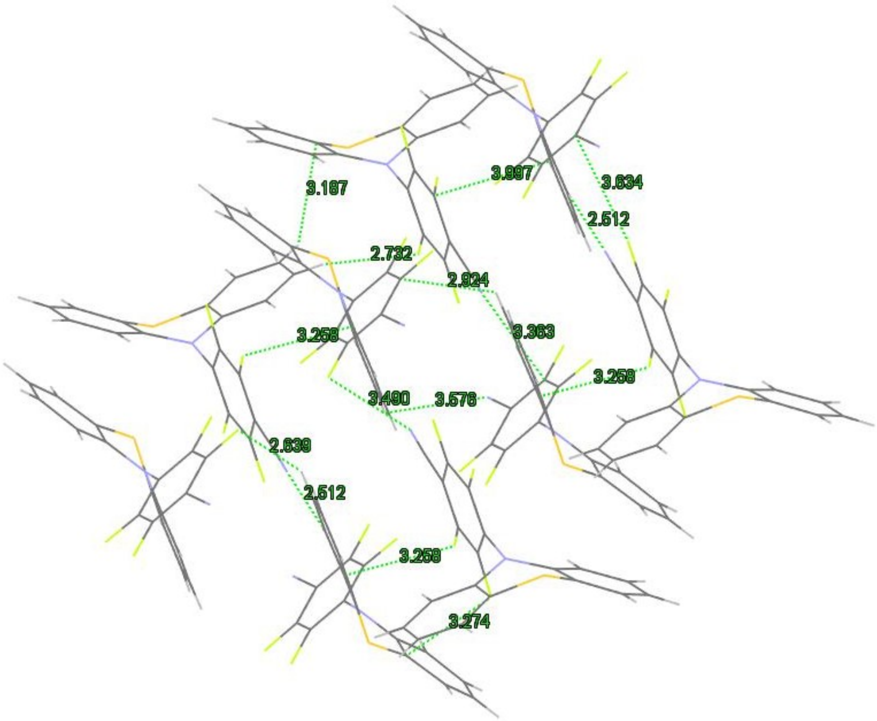

Figure S7: *Molecular packing with intermolecular interactions in crystal* ***Pht-BzN.***

3.2 GRAZING INCIDENCE WIDE-ANGLE X-RAY SCATTERING (GIWAXS) ON PHT-BZN MICROCRYSTALS

Grazing Incidence Wide-Angle Scattering (GIWAXS) measurements were performed at the XMI-Lab[15], equipped with a Fr-E+ Superbright X-ray micro-source (Rigaku) coupled to a SMAX3000 SAXS/WAXS camera through a focusing optics and a three-pinhole beam shaping system. A Fuji Image Plate was used as detector, placed downstream the sample at a 20 cm distance, and off-line read by a Raxia scanner. Data were calibrated, by using Ag Behenate (deposited as a thin film) powder standard, and processed by using the in-house developed program SUNBIM (freely available at http://www.ic.cnr.it/software/sunbim/)[16]. A flat detector correction was applied as implemented in SUNBIM, without any baseline interpolation. A high-precision goniometer with piezoelectric motors was used for sample alignment in GIWAXS measurements: the incidence angle was set to 0.18° to avoid scattering contribution from the substrate. Samples were kept at about 0.1 mbar vacuum pressure during measurements.

Results and discussions

The solution containing **Pht-BzN** crystals was casted on a silicon substrate and the solvent (water) was allowed to evaporate in the sample chamber at 0.1 mbar vacuum pressure to allow the detection of clear diffraction signals from the crystals (no signal could be visible before water evaporation).

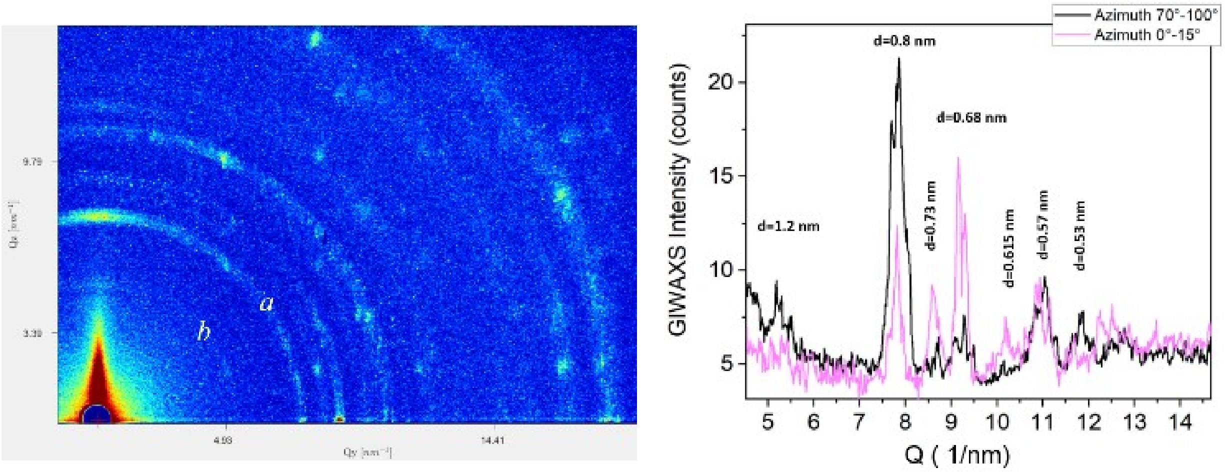

Fig. S8: *2D (left) and 1D (right) GIWAXS pattern of* ***Pht-BzN*** *microcrystals deposited on a silicon substrate, after water evaporation, as a function of the momentum transfer* $Q=(4\pi/\lambda)\sin\theta$ *(*λ *is the X-ray wavelength and* θ *the Bragg angle). The 1D cuts were extracted in the directions perpendicular (black curve) and parallel (magenta curve) to the substrate, showing the preferred orientations of the crystals.*

A spotty pattern can be observed, composed of continuous diffraction rings crossing the spots, indicating presence of large crystals laying on the substrate with a preferred crystallographic orientation together with several other crystals with random orientation and the same lattice structure. According to **Table S1**, the *a* and *b* axes can be recognized as the inner rings labeled on the 2D pattern in Figure S8 GIWAXS (left). On the other hand, the *c* axis is not visible, because of its large lattice parameter out of the accessible reciprocal space (smaller scattering angles or momentum transfer). A closeup of the d-spacings detected is reported in the 1D plots of Figure S8 GIWAXS (right), extracted in the directions parallel and perpendicular to the substrate.

3.3 ELECTROCHEMISTRY

Cyclic voltammetry (CV) experiments have been performed on all three donor-acceptor benzonitrile derivatives and the results are shown in **Fig. S9**. They feature an irreversible reduction peak, which can be assigned to reduction of the BzN core. Furthermore, they present one or two oxidation peaks, which can be assigned to the donor moieties. It is important to note that **Phx-BzN** and **Pht-BzN** both oxidize quasi-reversibly (**Fig. S9b**, **S9c**), while the oxidation of the **Cz-BzN** is irreversible (**Fig. S9a**). The peak ratio between the first oxidation and first reduction is about 1.73 for **Phx-BzN** and 2.2 for **Pht-BzN**. Both correspond to the one-electron oxidation of phenoxazine and phenothiazine, therefore the reduction of benzonitrile is bielectronic, as already reported and discussed previously.[11]

The summary of redox potentials as well as the corresponding HOMO and LUMO values are given in **Table S3**. Interestingly, the results obtained suggest phenothiazine has a slightly larger donor strength than phenoxazine. This is in disagreement with the HOMO energies obtained from DFT calculations (below) and with the oxidation potentials of the *N*-methyl derivatives of the three donors reported in literature[17-19].

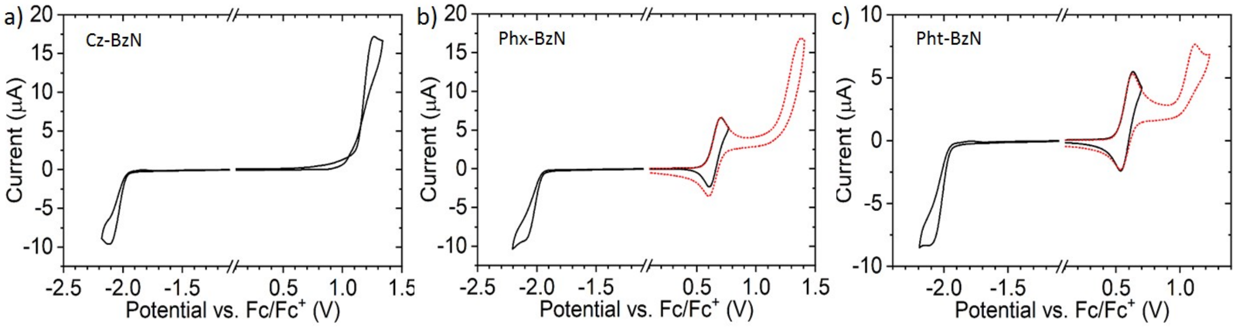

Figure S9: *CV traces of (a)* ***Cz-BzN,*** *(b)* ***Phx-BzN,*** *(c)* ***Pht-BzN.*** *The vertex potential in oxidation is set to 0.8 V (black trace) or 1.4 V (red trace).*

Table S3: Summary of electrochemical redox potentials and HOMO and LUMO energy.

	E_{ox} *vs.* Fc/Fc+ (V)$^{(a)}$	**E_{red} *vs.* Fc/Fc+ (V)$^{(a)}$**	**Cathodic to anodic peak current ratio**	**Number of electrons**	**HOMO (eV)$^{(b)}$**	**LUMO (eV)$^{(c)}$**	**HOMO-LUMO (eV)**
Cz-BzN	1.12	-1.98	/	irreversible	-6.22	-3.12	3.10
Phx-BzN	0.58	-1.96	1.73	1	-5.68	-3.14	2.54
Pht-BzN	0.51	-1.96	2.2	1	-5.61	-3.14	2.47

(a) Measured in DCM at room temperature by cyclic voltammetry. (b) Estimated from the oxidation potential in DCM, HOMO = $-E_{ox} - 5.1$; (c) Estimated from the reduction potential in DCM, LUMO = $-E_{red} - 5.1$.

3.4 DFT CALCULATIONS

Ground state geometries were optimized at the PBE0/6-31+g(d,p) level of calculation followed by a frequency calculation. TDDFT on these geometries were done at the PBE0/6-311+g(d,p) level of theory looking for both singlets and triplet levels including toluene solvent effect with IEFPCM model. Then first singlet and triplet excited state geometries were optimized independently at the PBE0/6-31+g(d,p) level followed by a frequency calculation at the same level. Finally, a TDDFT calculation was done on these S_1 and T_1 optimized geometries at the PBE0/6-311+g(d,p) level of theory looking for both singlets and triplets levels including toluene solvent effect with IEFPCM model. For all geometries frequency calculations gave only real values confirming that all structures are true minima. All calculations were done with Gaussian 16 (Revision B.01) software.[20] Data were analyzed with GaussView 6.0 (molecular orbitals), PyMOL (The PyMOL Molecular Graphics System, Version 2.1.1 Schrödinger, LLC; molecular structures overlay plots), Mercury 4.1.0 (angles measurements), GaussSum3.0[21] (energy levels of molecular orbitals).

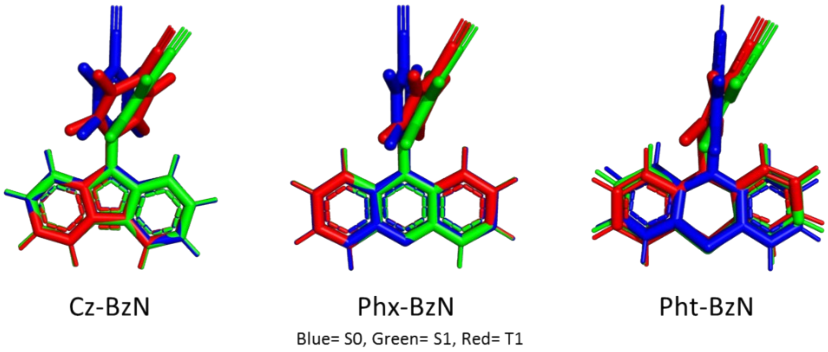

Figure S10: *Optimized structures in the ground and excited states of, from left to right **Cz-BzN** (blue=S_0, green=S_1, red=T_1), **Phx-BzN** (blue=S_0, green=S_1, red=T_1) and **Pht-BzN** (blue=S_0, green=S_1, red=T_1).*

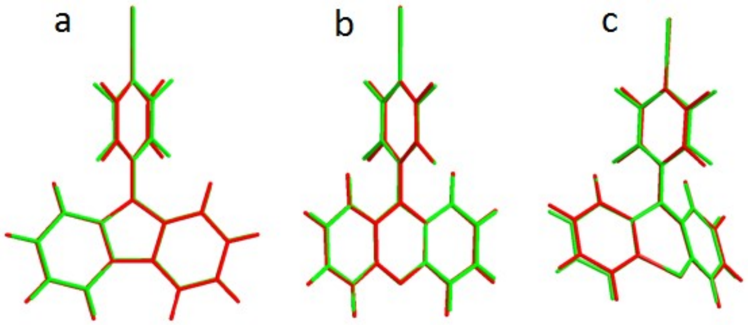

Figure S11: *Overlap between the calculated and XRD structures* of (a) ***Cz-BzN,*** *(b)* ***Phx-BzN,*** *(c)* ***Pht-BzN****, colors: red = calculated, green = X-Ray.*

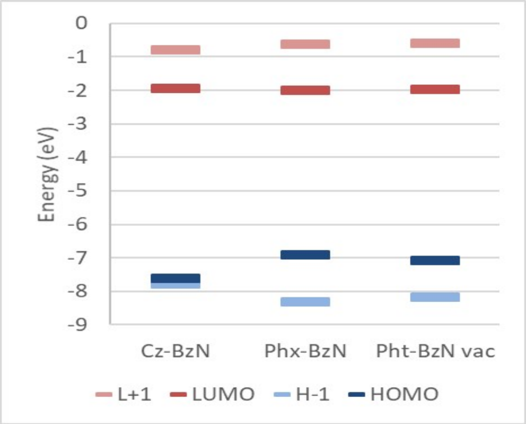

Figure S12: *Representation of the energy levels of the frontier molecular orbitals of* **Cz-BzN, Phx-BzN,** and **Pht-BzN**.

Table S4: Energies in eV of the calculated frontier MOs.

	Cz-BzN	**Phx-BzN**	**Pht-BzN**
LUMO+1	-0.79	-0.63	-0.6
LUMO	-1.95	-2.01	-1.98
HOMO	-7.62	-6.92	-7.09
HOMO-1	-7.77	-8.31	-8.17

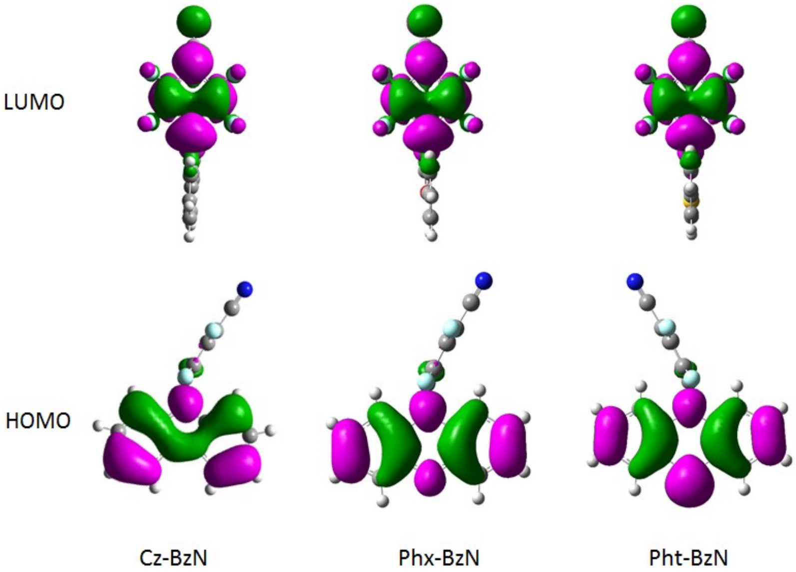

Figure S13*: Electron density distributions in molecular orbital energy levels involved in the HOMO-LUMO calculated transition in the* S_1 *molecular geometry, of (from left to right)* ***Cz-BzN****,* ***Phx-BzN****,* ***Pht-BzN****.*

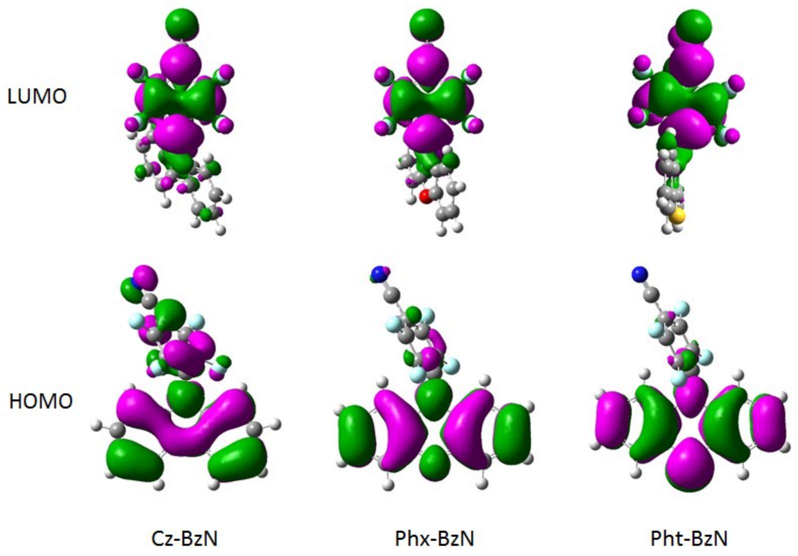

Figure S14: *Electron density distributions in molecular orbital energy levels involved in the HOMO-LUMO calculated transition in the T_1 molecular geometry, of (from left to right)* ***Cz-BzN***, ***Phx-BzN***, ***Pht-BzN***.

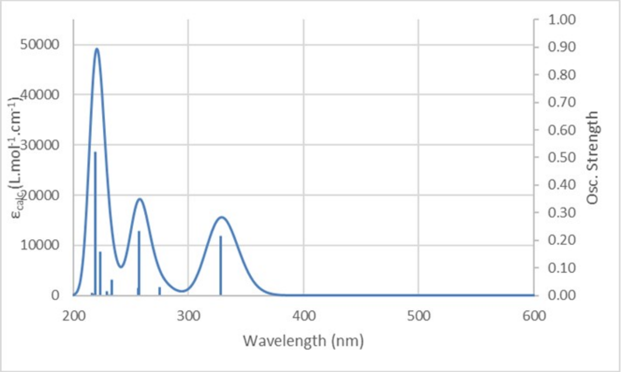

Figure S15: *Calculated spectra and transitions of* ***Cz-BzN***.

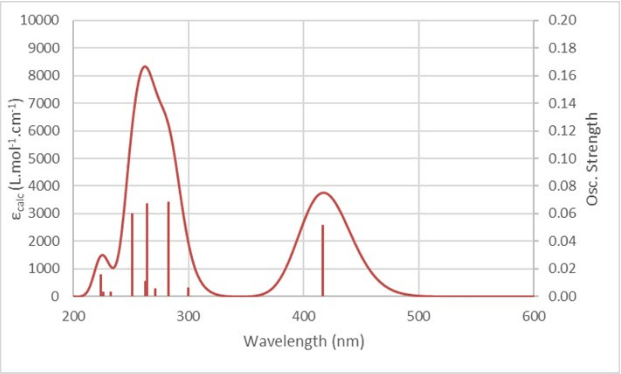

Figure S16: *Calculated spectra and transitions of* ***Phx-BzN***.

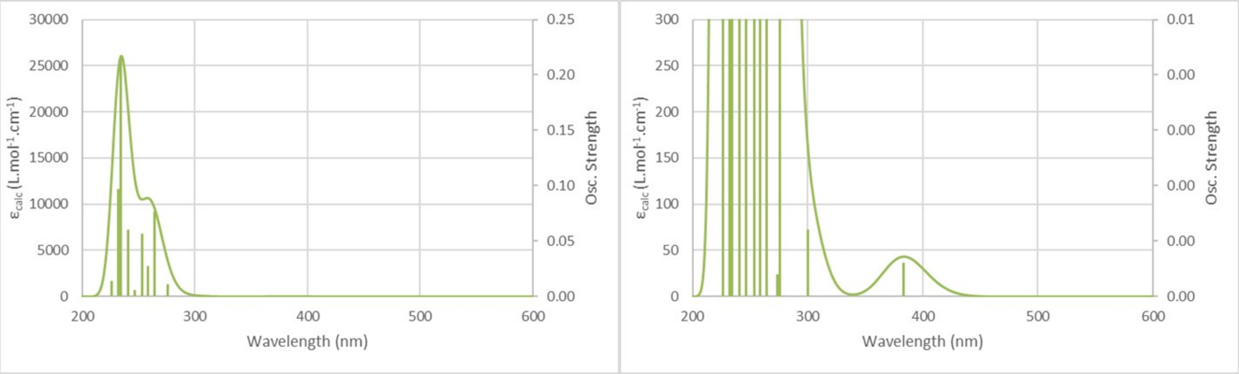

***Figure S17**: Calculated spectra and transitions of **Pht-BzN**. The calculated oscillator strength of the first CT of **Pht-BzN** is very small so the band is weak (close-up on the right).*

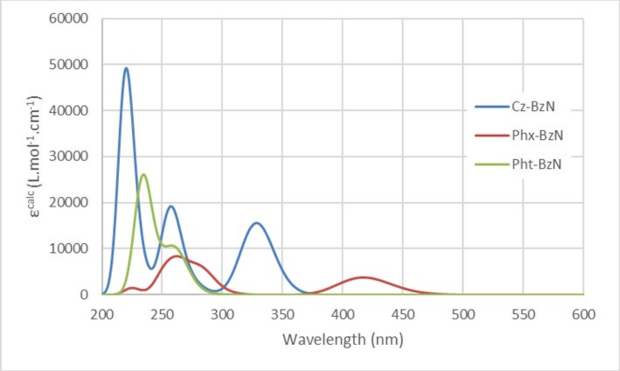

***Figure S18**: Overlay of calculated spectra of **Cz-BzN** (blue), **Phx-BzN** (red) and **Pht-BzN** (green).*

Table S5: Calculated (TDDFT) absorption maximum wavelengths (in nm) compared with experimental values.

	TDDFT	**Cyclohexane**	**DCM**	**PMMA**
Cz-BzN (abs)	«329v	354	344	350
Phx-BzN (abs)	419	421	414	407
Pht-BzN (abs)	385	395	385	385

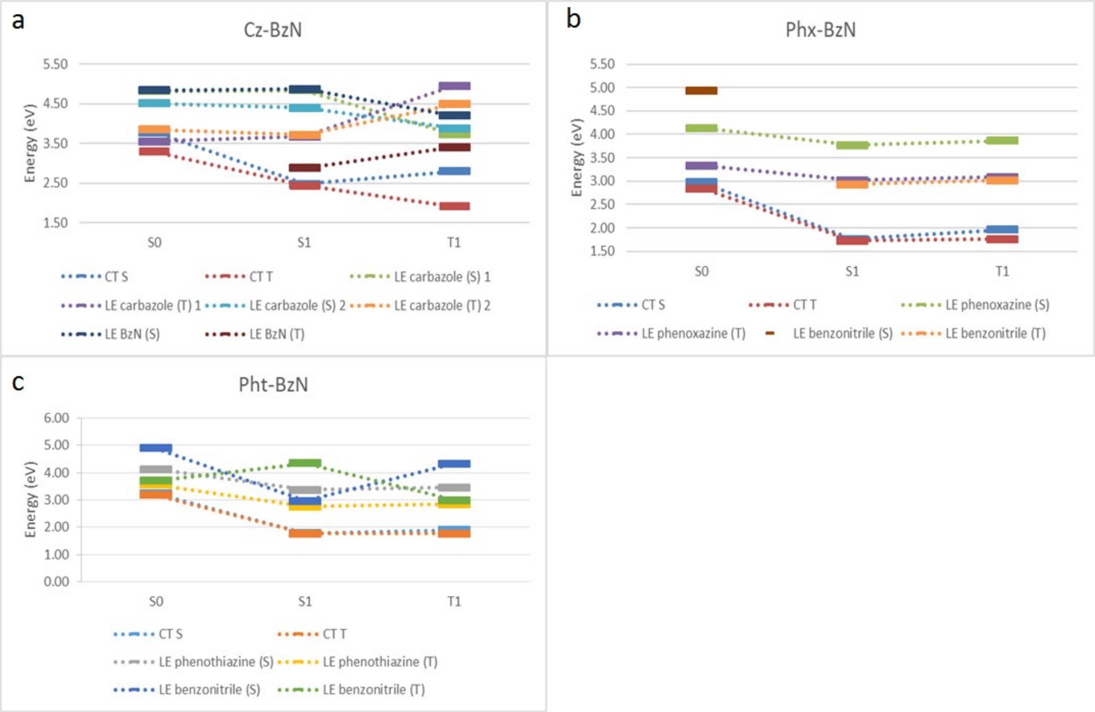

Figure S19*: Energy diagram of the triplet and singlet LE and CT states, for* ***a) Cz-BzN*** *and* ***b) Phx-BzN c) Pht-BzN*** *molecules in the S_0, S_1 and T_1 geometry configuration, obtained with DTF calculations.*

Table S6: Energy difference between S_1 and T_1 (ΔE_{ST}) in eV obtained from the calculations of the molecules in S_0, S_1 and T_1 geometry configuration.

	ΔE_{ST} (S_0)	**ΔE_{ST} (S_1)**	**ΔE_{ST} (T_1)**
Cz-BzN	0.49	0.03	0.89
Phx-BzN	0.13	0.03	0.20
Pht-BzN	0.06	0.02	0.13

Table S7: Calculated energy values of the first energy transitions at the ground state (S_0), first singlet excited (S_1) and first triplet (T_1) geometries for **Cz-BzN, Phx-BzN**, and **Pht-BzN** in vacuum.

	S_0 (ground state geometry)				**S_1 (excited state geometry)**				**T_1 (excited state geometry)**				
	S (eV)	**T (eV)**	**f(S_n)**	**Transition**	**S (eV)**	**T (eV)**	**f(S_n)**	**Transition**	**S (eV)**	**T (eV)**	**f(S_n)**	**Transition**	
Cz-BzN	3.78	3.29	0.2155	H->L	2.47	2.44	0.0002	H->L	2.80	1.91	0.2682	H->L	CT
Cz-BzN	4.82	3.55	0.2328	H-1->L+1	4.84	3.67	0.1162	H-4->L	-	3.72	0	H-1->L+1	LE Cz
Cz-BzN	4.51	3.85	0.0308	H->L+1	4.39	3.71	0	H->L+1	-	3.88	0	H->L+1	LE Cz
Cz-BzN	4.84	-	0.0281	H-3->L	4.87	2.88	0.4314	H-4->L	4.20	3.40	0.0352	H-3->L	LE BzN
Phx-BzN	2.97	2.84	0.052	H->L	1.76	1.73	0	H->L	1.96	1.76	-	H->L	CT
Phx-BzN	4.13	3.33	0.0064	H->L+3	3.77	3.01	0.0111	H->L+1	3.86	3.09	-	H-1->L+3	LE Phx
Phx-BzN	4.93	3.77	0.0604	H-4->L	-	2.93	0	H-4->L		3.02	-	H-4->L	LE BzN
Pht-BzN	3.24	3.18	0.0006	H->L	1.79	1.77	0	H->L	1.90	1.77	0.0297	H->L	CT
Pht-BzN	4.13	3.56	0.0012	H->L+3	3.37	2.76	0	H->L+1	3.46	2.85	0.0005	H->L+3	LE Pht
Pht-BzN	4.89	3.70	0.0565	H-4 ->L	4.34	3.42	0.0454	H-5 ->L	-	3.42	0	H-4->L	LE BzN

3.5 PHOTOPHYSICS

3.5.1 Steady state photophysical properties

Table S8: Emission wavelengths and FWHM of **Cz-BzN**, **Phx-BzN** and **Pht-BzN**.

	λ_{PL} (nm)	FWHM (nm)
Cz-BzN PMMA	423	101
Cz-BzN crystal	439	62
Phx-BzN PMMA	532	131
Phx-BzN crystal	588	104
Pht-BzN PMMA	553	143
Pht-BzN crystal	487	96

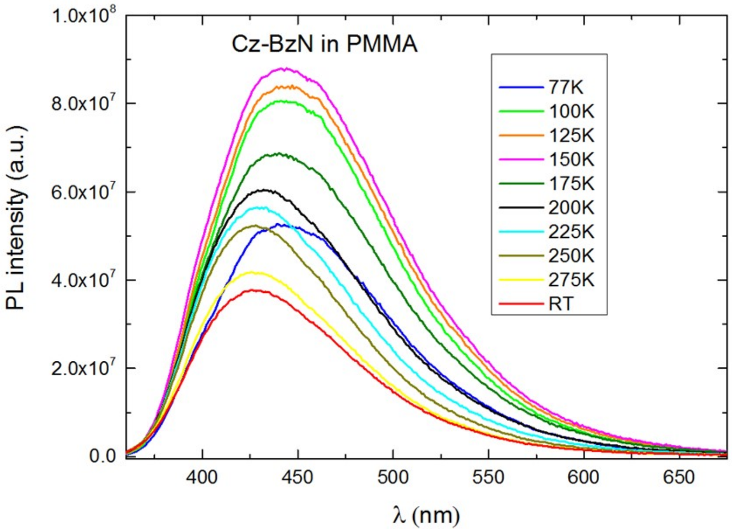

Figure S20*: Steady state emission of* ***Cz-BzN*** *in PMMA (degassed) at different temperatures from 77 K to RT.* λ_{ex}*= 330nm*

Table S9: Estimated PLQY of **Cz-BzN** in PMMA at different temperatures from 77K to 275K.
(PLQY at RT calculated with integration sphere)

	80K	100K	125K	150K	175K	200K	225K	250K	275K	RT
PLQY(%)	58.0	88.9	97.2	100	78.1	65.6	57.4	51.2	40.9	39.0

(for all Φ_{PL}, the experimental error is ±20% of the value)

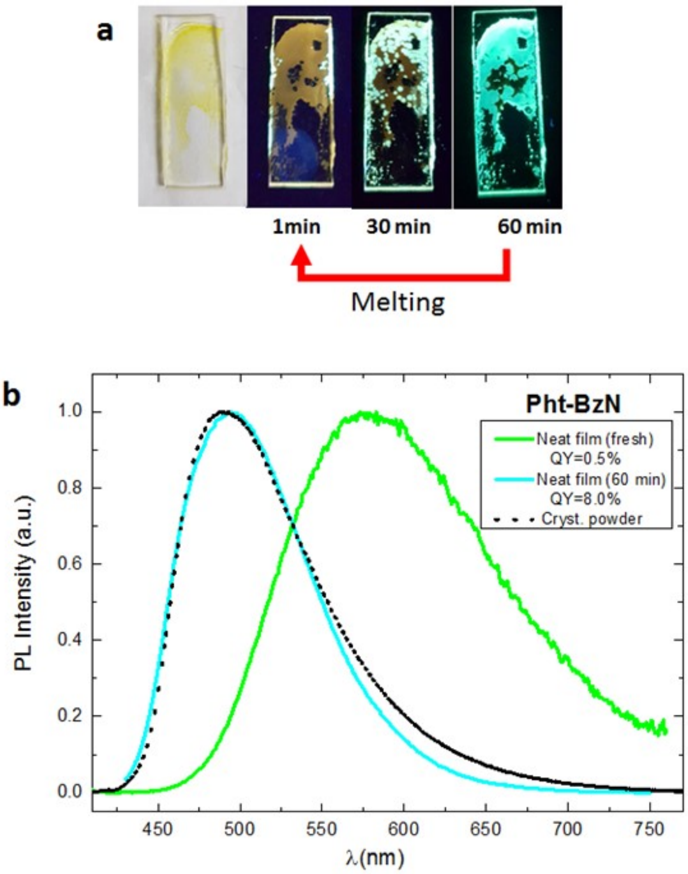

***Figure S21**: **a)** fluorescence images of **Pht-BzN** neat film after 1 min, after 30 min, and after 60 min. Melting the **Pht-BzN** neat film after crystallization is obtained the initial (neat 1 min) amorphous emission. **b)** Normalized photoluminescence (PL) spectra of **Pht-BzN** in neat film obtained from DCM solution fresh (0-3 min), neat film crystallized (60 min) compared with crystalline powder.*

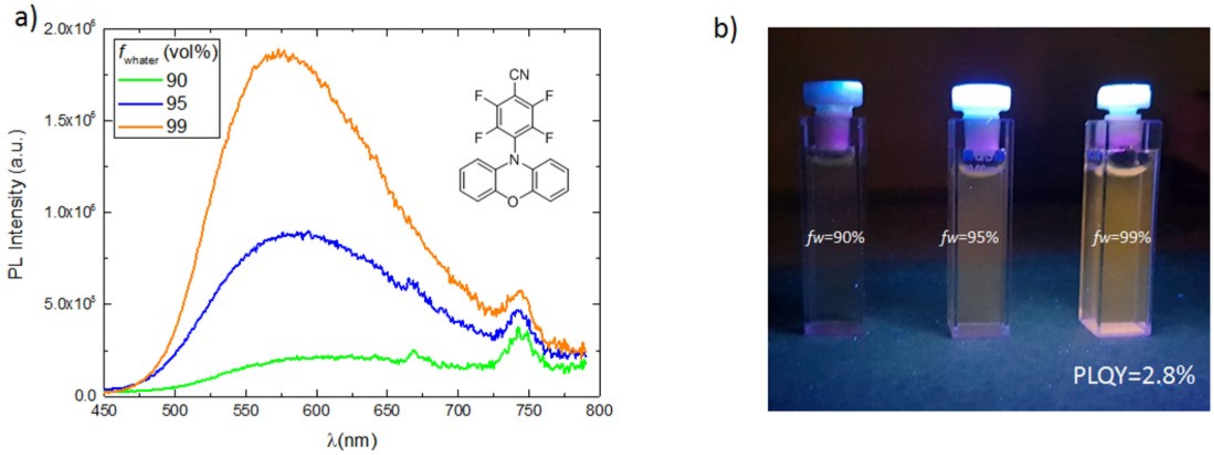

***Figure S22**: **a)** PL spectra of **Phx-BzN** in THF/water mixtures with different water fractions (f_w). **b)** Pictures of **Phx-BzN** in different THF/water mixtures (f_w=90, 95 and 99% from left to right) under UV light (365nm) irradiation.*

3.5.2 Time resolved photophysical properties

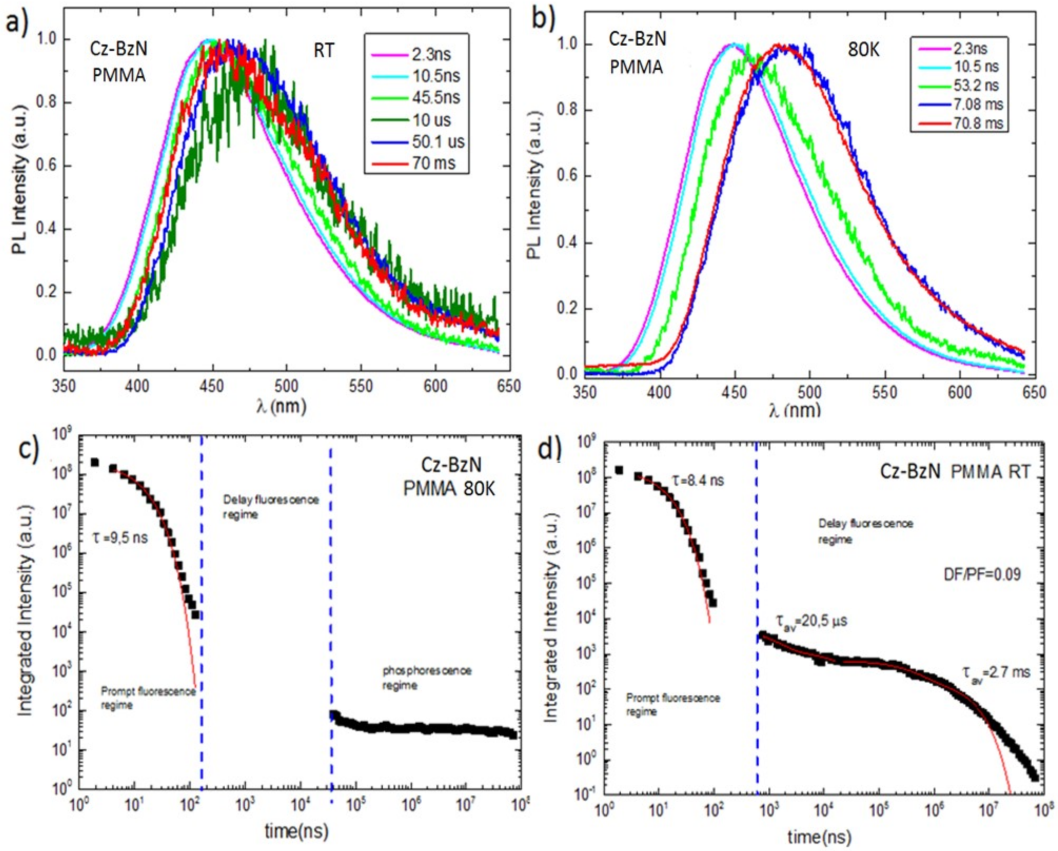

***Figure S23**: **a)** Time-resolved emission spectra of **Cz-BzN** in PMMA at room temperature (RT) **b)** time-resolved emission spectra of **Cz-BzN** in PMMA at 80K. **c)** Decay curve and fitting of **Cz-BzN** in PMMA at 80K. **d)** Decay curve and fitting of **Cz-BzN** in PMMA at RT. All samples were prepared at a concentration of 0.05 wt% in PMMA. For all measurements λ_{ex}= 355 nm.*

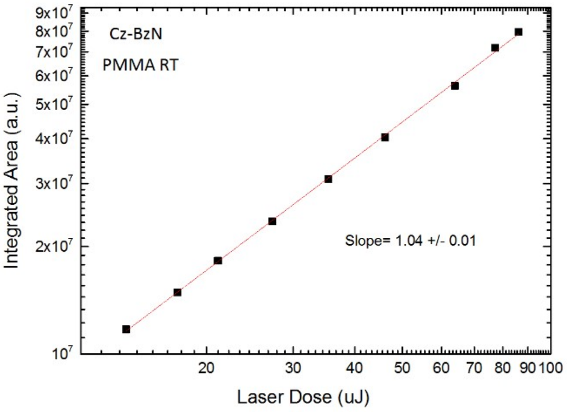

***Figure S24**: Intensity dependence of the DF emission as a function of the laser excitation dose for **Cz-BzN** in PMMA at RT. λ_{ex}= 337 nm.*

The **Cz-BzN** crystalline powder shows only prompt fluorescence at room temperature (**Fig. S25a**). The photoluminescence recorded at early delay times undergoes a slight blue shift in the first 3 nanoseconds, likely because the initial LE contribution of D or A shifts the CT emission spectrum towards higher energy. At longer delay time, no delayed fluorescence can be detected. DFT calculations show that at the S_0 geometry the compound has a relatively small D-A angle allowing a partial delocalization of HOMO on both donor and acceptor moieties, leading to a large ΔE_{ST}. In this case the S_0 geometry is retained in the excited state due to the rigid environment of the crystal, thus a large ΔE_{ST} = 0.47 eV. This behaviour is different from the less rigid environment of PMMA and solution, where relaxation of the excited state geometry is allowed, thus leading to a smaller ΔE_{ST} and TADF. At 80K (**Fig. S25b**), the highly vibronic long-lived emission at later delay times, ~ms, shows a significant red shift in respect to prompt fluorescence. This photoluminescence, which can be attributed to phosphorescence, shows an onset energy lower by 0.47 eV than the triplet energy of carbazole (3.20 eV) (**Fig. S25c**). Such discrepancy between T_1 energy of **Cz-BzN** in crystal and T_1 of carbazole suggests the triplet state of the former should be stabilised by either delocalisation within one molecule or due to intermolecular interactions. DF that appears to be present at 80 K at intermediate delay time (between phosphorescence and prompt fluorescence regimes) can be assigned most likely to triplet-triplet annihilation (TTA).

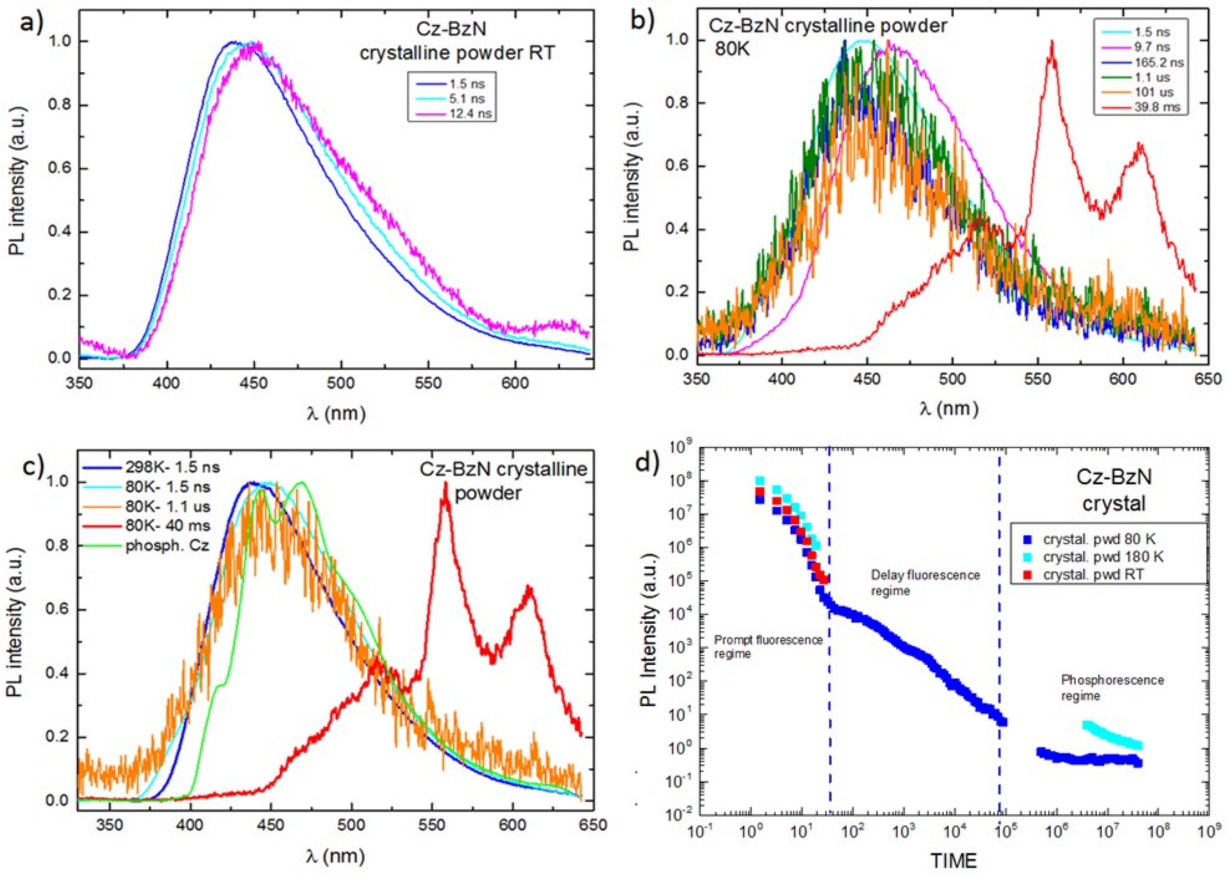

***Figure S25**: **a)** Time-resolved emission of **Cz-BzN** crystalline powder at room temperature (RT) **b)** time-resolved emission of **Cz-BzN** crystalline powder at 80K **c)** time-resolved emission spectra of **Cz-BzN** at RT and 80K with phosphorescence of carbazole **d)** decay curve profile of **Cz-BzN** crystalline powder at RT, 180K, and 80K, and for neat film at RT. All experiments were carried out with λ_{ex}= 355 nm.*

3.5.3 Time resolved photophysical properties of Phx-BzN crystalline powder

The time-resolved emission properties of **Phx-BzN** crystalline powder were studied at four different temperatures: RT (**Fig. S26a**), 200K (**Fig. S26c**), 140K (**Fig. S26e**) and 80K (**Fig. S27a**). At each temperature the spectra remain invariant with increasing delay time, but a strong blue shift of the emission occurs when the temperature decreases. For each temperature the emission lives up to several microseconds, thus demonstrating properties typical for delayed fluorescence. In **Fig. S28a** are shown the PF emission spectra at each temperature, and we can see that the emission moderately blue shifts when the temperature decreases, while the PL spectra become narrower. At 80K, we observe weak vibronic progression to the PF spectrum. Cooling **Phx-BzN** crystals to 80K and heating back to RT results in the sample having different physical form and displaying different photophysical behaviour than the original crystals. This behaviour might be due to formation of a new polymorph. We observe that the PL decay of **Phx-BzN** (**Fig S28b**) can be fitted with two monoexponential expressions: one for PF and the other for DF. The intensity dependence of the DF emission as a function of laser excitation dose for **Phx-BzN** crystalline powder at RT (**Fig. S29**) confirms a monomolecular mechanism at work typical of thermally-activated delayed fluorescence. It is worth of note that also the decay at 80K shows long-lived and moderately intense TADF emission. As TADF phenomena require thermal energy to be activated, the singlet-triplet energy gap must be approaching zero. At 80 K the non-radiative decay is also suppressed allowing to observe a very long decay time of 513 μs (**Table S10**), three orders of magnitude longer than that at RT (0.2 μs). The DF/PF ratio calculated from the decay profile at RT (**Table S10**) shows that the contribution of TADF is nearly five-fold larger in crystal than in PMMA.

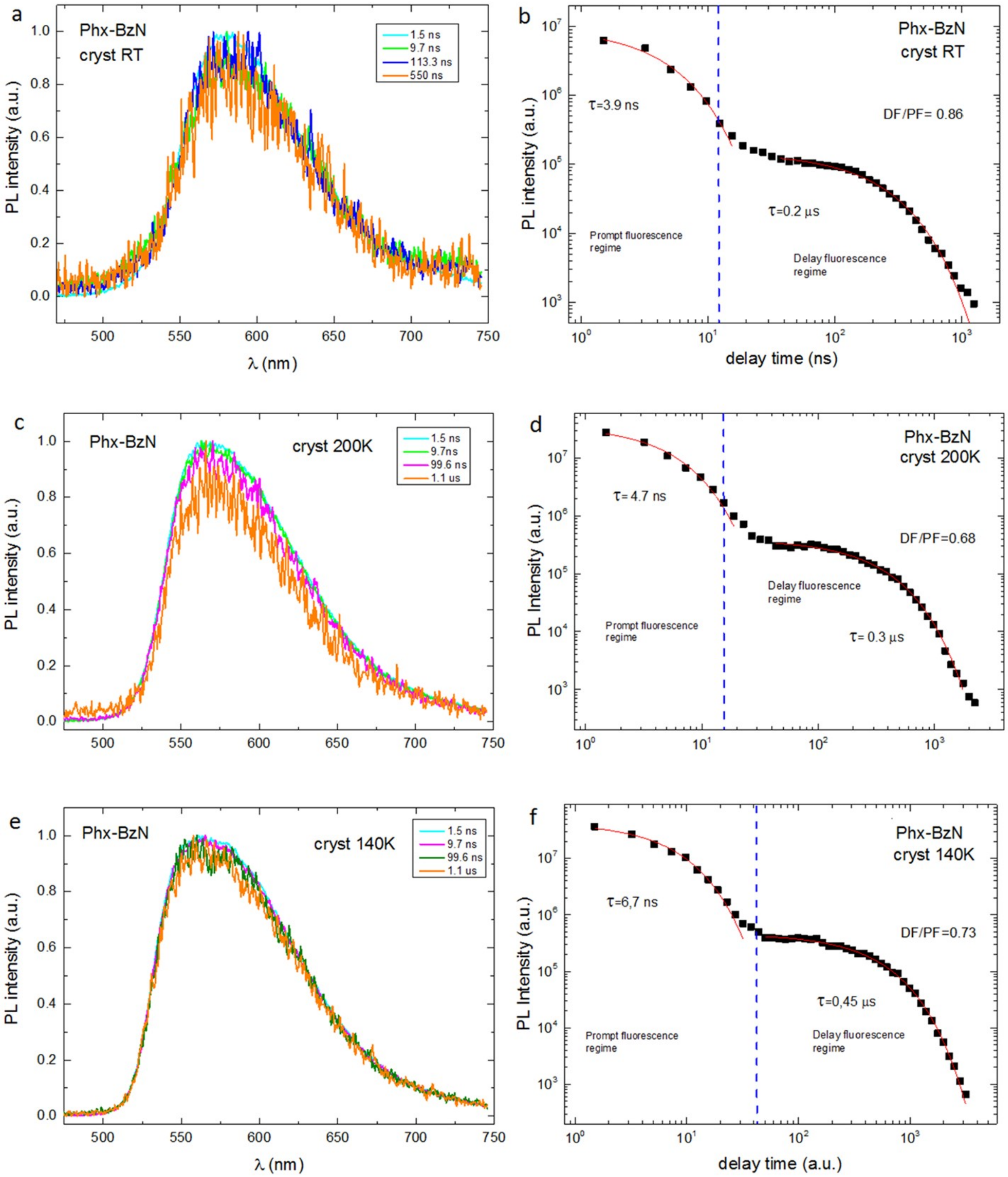

***Figure S26**: Time-resolved emission spectra of **Phx-BzN** crystal powder at **a)** RT **c)** 200K and **e)** 140K. Decay curve and fitting of **Phx-BzN** crystal powder for **b)** RT and **d)** 200 K and **f)** 140K. All experiments were carried out at λ_{ex}= 355 nm.*

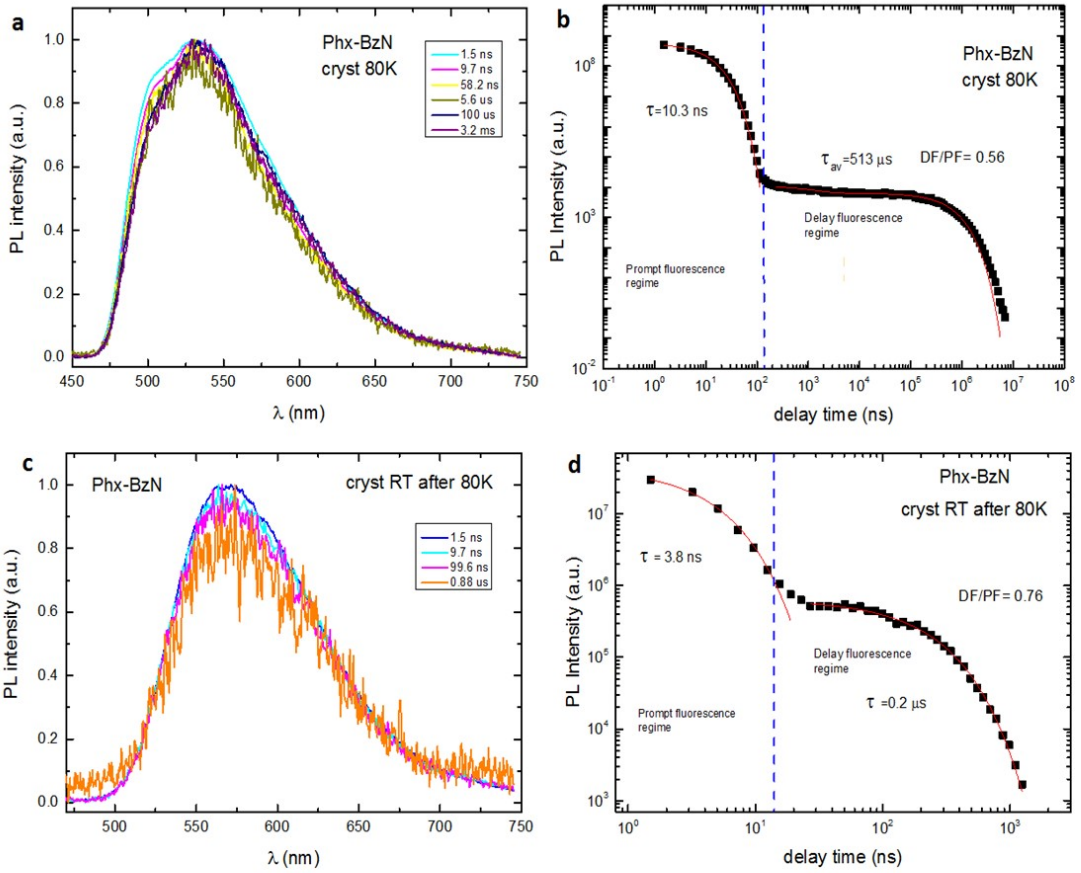

***Figure S27**: Time-resolved emission spectra of **Phx-BzN** crystal powder at **a)** 80K **c)** RT after cooling at 80K; decay curve and fitting of **Phx-BzN** crystal powder for **b)** 80K and **c)** RT after cooling at 80K. All experiments were carried out at λ_{ex}= 355 nm.*

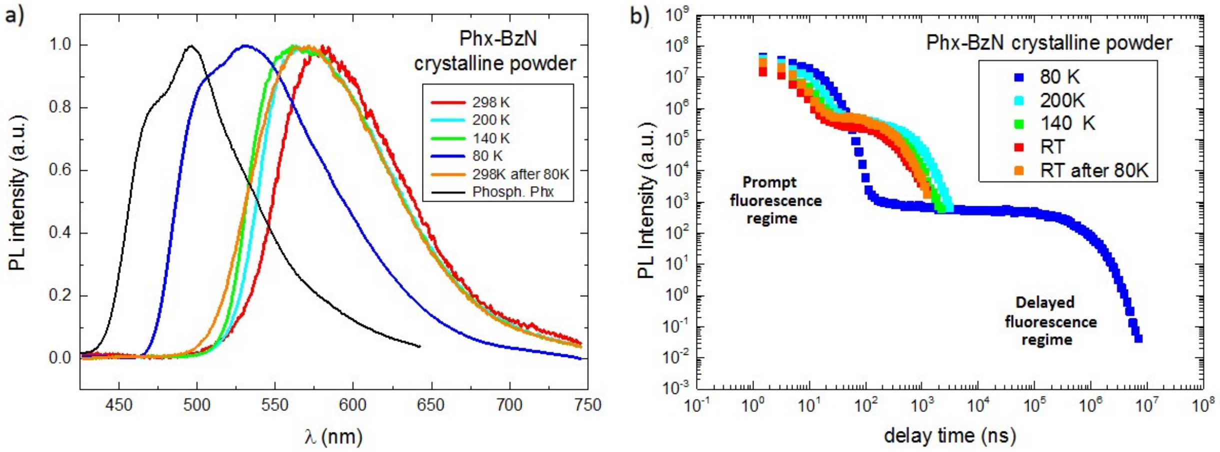

Figure S28**: **a)** Time-resolved emission spectra of **Phx-BzN** crystalline powder for RT, 200K, 140K, 80K and RT after 80K, from the early prompt emission (same for longer TD) 80K in comparison with* *phosphorescence of Phenoxazine.* ***b) *Decay curve profile of* ***Phx-BzN*** *crystalline powder for RT, 200K, 140K, 80K and RT after 80K. All experiments were carried out at* λ_{ex}*= 355 nm.*

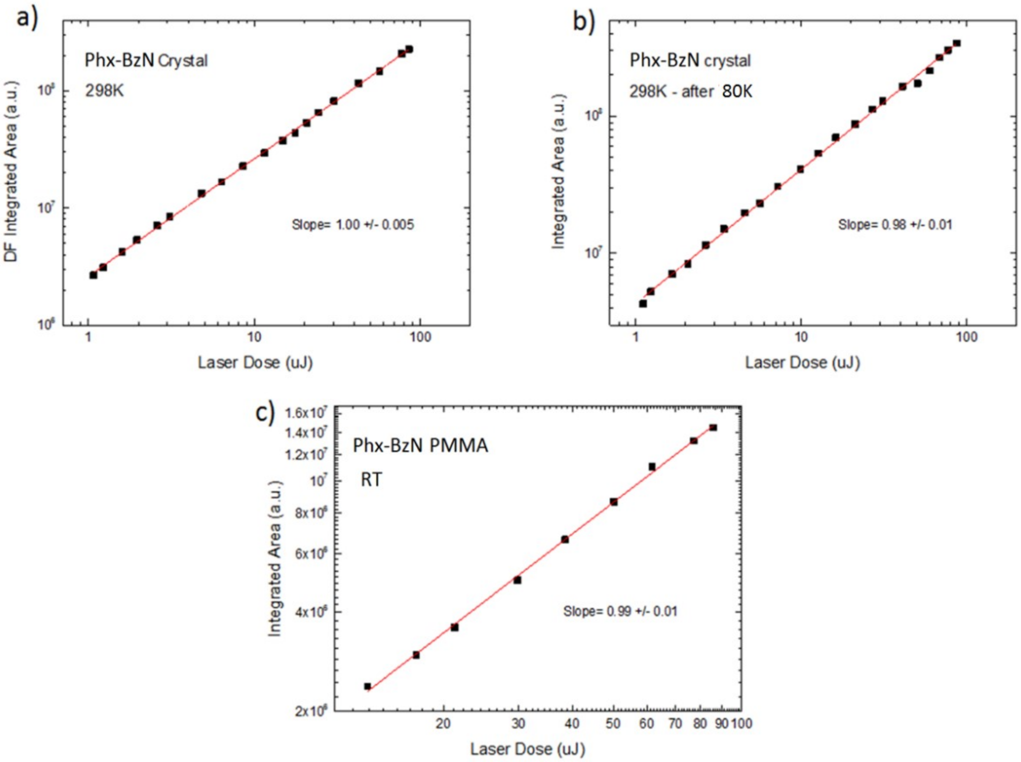

Figure S29: *Intensity dependence of the DF emission as a function of laser excitation dose for* ***a) Phx-BzN*** *crystal RT,* ***b) Phx-BzN*** *crystal RT after 77K,* ***c) Phx-BzN*** *neat film at RT, and* ***d) Phx-BzN*** *in* ***PMMA*** *at RT.* λ_{ex}*= 337 nm.*

Table S10: Photophysical properties of **Phx-BzN**

	λ_{PL} (nm)	**$\Phi_{PL}{}^{air}/\Phi_{PL}{}^{deoxyg}$**	**τ_{PF} (ns)**	**τ_{DF} (µs)**	**$\Delta E_{S-T}{}^{c}$ (eV)**	**DF/PF^{d}**
Phx-BzN Crystal RT	580	0.05	3.9	0.20	-	0.86
Phx-BzN Crystal RT after 80K	570	n.c.	3.8	0.20	-	0.76
Phx-BzN Crystal 200K	563	0.22^{a}	4.7	0.29	-	0.68
Phx-BzN Crystal 140K	560	0.38^{a}	6.7	0.45	-	0.73
Phx-BzN Crystal 80K	506/532	-	10.3	513^{b}	0.00	0.56

$^{(deoxyg)}$ oxygen-free conditions, $^{(a)}$ PLQY estimated by comparing the PL intensity at RT with that at 200 or 140K, * average decay lifetime from biexponential fit. (The determination of the average decay time is described in §1.4). $^{(c)}$ calculated from the onset of the delayed fluorescence and phosphorescence spectra. $^{(d)}$ Delayed fluorescence to prompt fluorescence ratio derived as a ratio of integrated delayed fluorescence (DF) and prompt fluorescence (PF) intensity from the fitted decay curves. For all Φ_{PL} the experimental error is ±20% of the value.

3.5.4 Time resolved photophysical properties of Pht-BzN

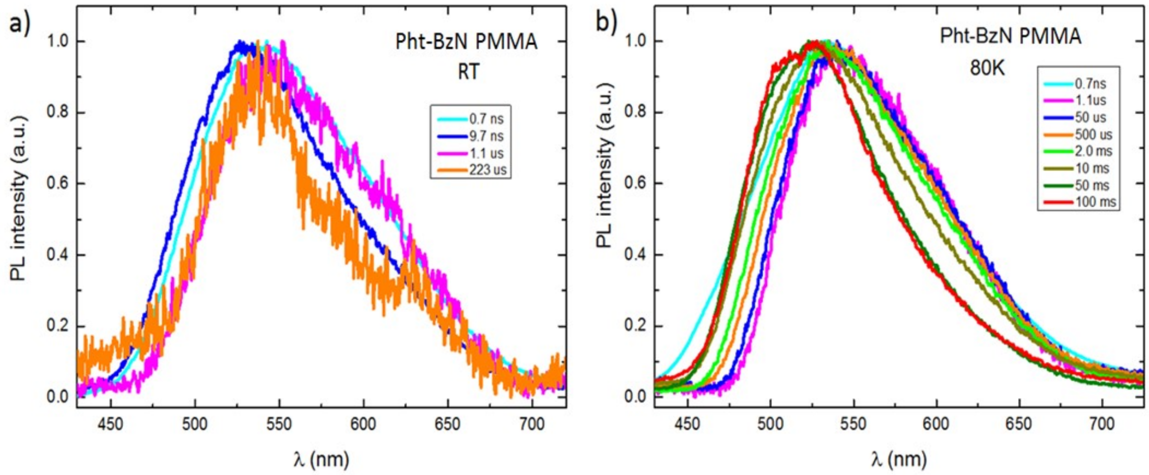

Figure S30: ***a)*** *Time-resolved emission spectra of* ***Pht-BzN*** *in PMMA (0.05wt%) at room temperature (RT)* ***b)*** *time-resolved emission spectra of* ***Pht-BzN*** *in PMMA (0.05wt%) at 80 K. All experiments were carried out with* λ_{ex}*= 355 nm.*

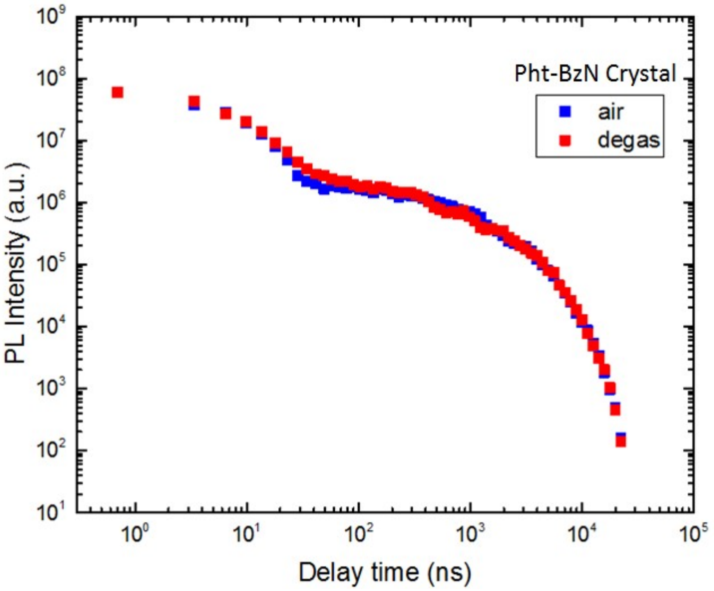

Figure S31: *PL decays of* ***Pht-BzN*** *crystal in degassed and air-equilibrated atmosphere at room temperature,* λ_{ex}*= 355 nm.*

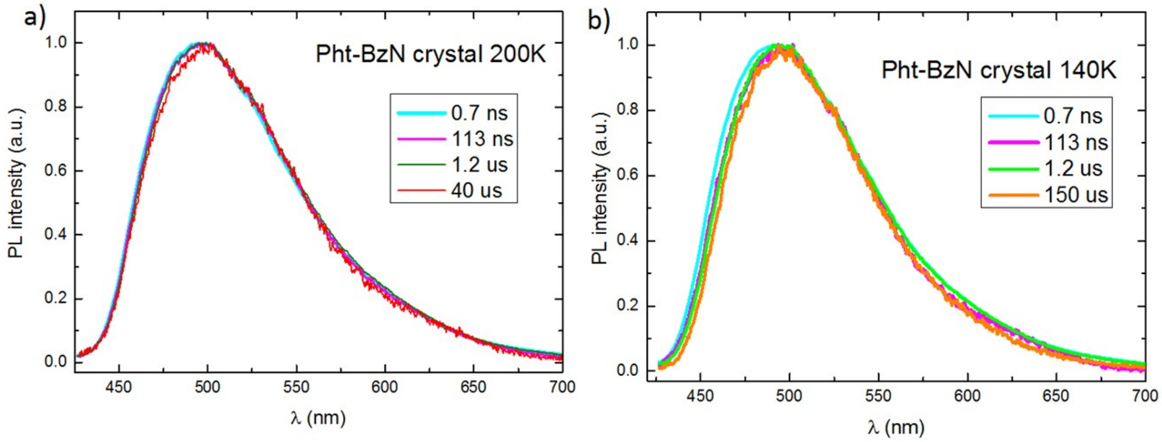

Figure S32: ***a)*** *time-resolved emission spectra of* ***Pht-BzN*** *crystal at 200K* ***b)*** *time-resolved emission spectra of* ***Pht-BzN*** *crystal at 140K, λ_{ex}= 355 nm.*

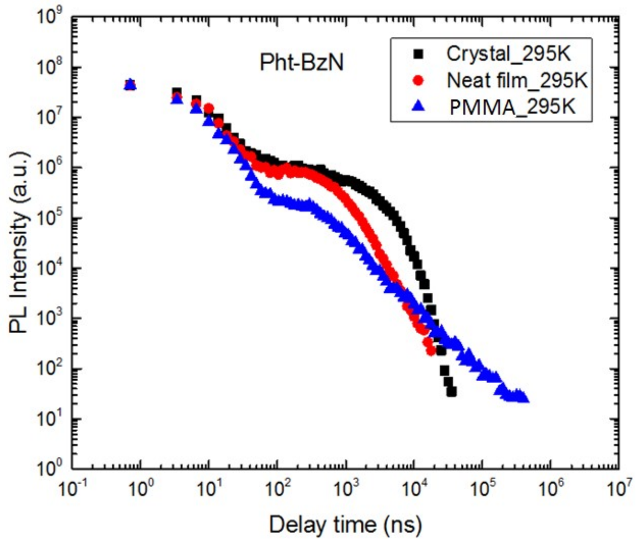

Figure S33: *Decay curves at RT of* ***Pht-BzN*** *in crystal, crystallized neat film, and in PMMA. λ_{ex}= 355 nm.*

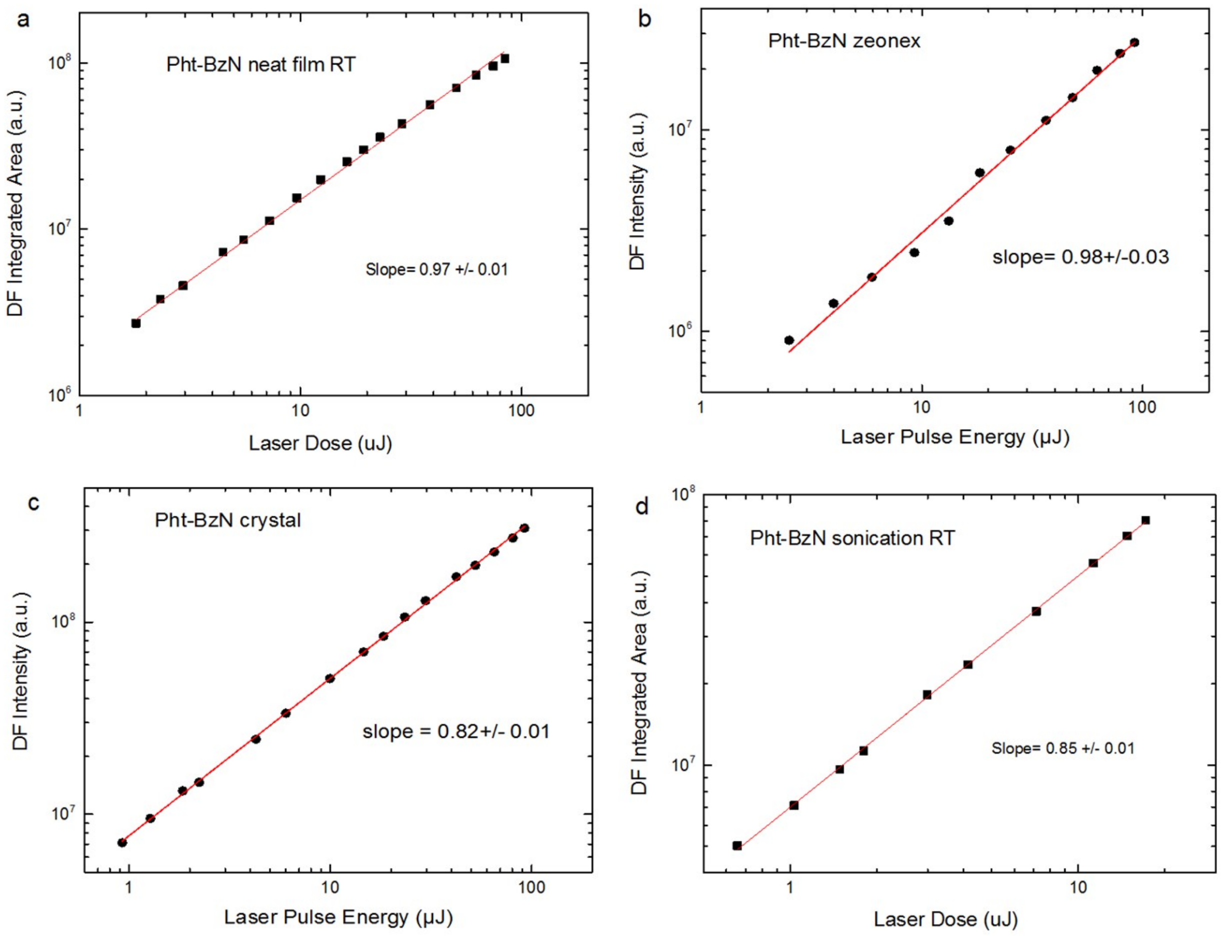

Figure S34: *Intensity dependence of the DF emission as a function of laser excitation dose for* ***Pht-BzN*** *at RT:* ***a)*** *PMMA at RT* ***b)*** *crystallized neat film at RT,* ***c)*** *crystal RT and* ***d)*** *crystalline dispersion obtained trough sonication.* λ_{ex}= *337 nm.*

3.6 DLS ANALYSIS

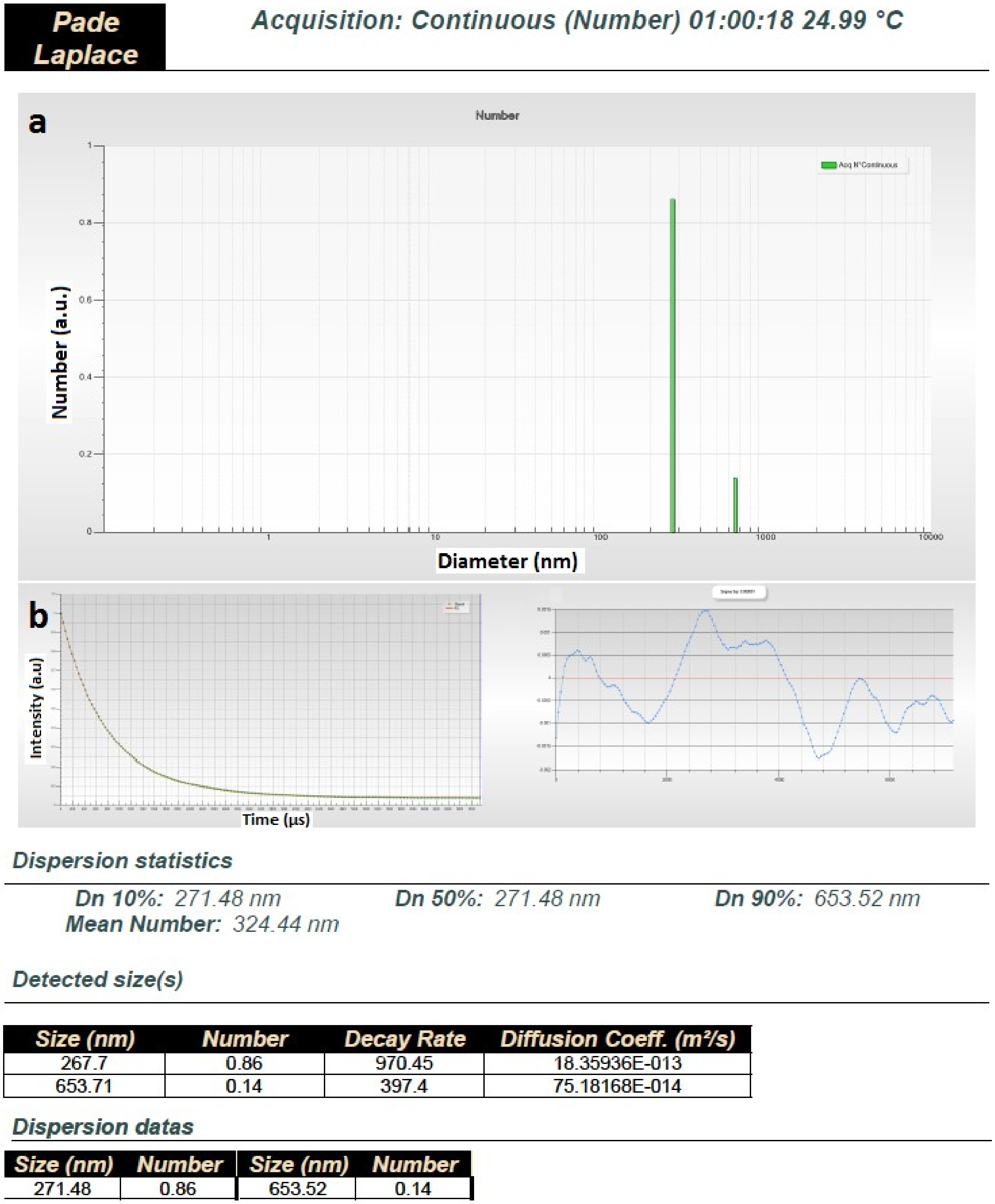

Pade Laplace

Acquisition: Continuous (Number) 01:00:18 24.99 °C

Dispersion statistics

Dn 10%: *271.48 nm* **Dn 50%:** *271.48 nm* **Dn 90%:** *653.52 nm*
Mean Number: *324.44 nm*

Detected size(s)

Size (nm)	Number	Decay Rate	Diffusion Coeff. (m²/s)
267.7	0.86	970.45	18.35936E-013
653.71	0.14	397.4	75.18168E-014

Dispersion datas

Size (nm)	Number	Size (nm)	Number
271.48	0.86	653.52	0.14

Figure S35: a) *Size histogram of the **Pht-BzN** microcrystal dispersion obtained with Padé-Laplace algorithm and the statistical acquisition mode. The horizontal axis shows the hydrodynamic diameter in nm and the vertical axis the amplitude in intensity (a.u.). **b)** Correlogram obtained from the **Pht-BzN** microcrystal dispersion, (green spots) and fit of the Padé-Laplace algorithm (red curve). In the Table are reported the dimensions of particle sizes obtained from the acquisition.*

3.7 NMR AND MS SPECTRA

Regarding peak assignments, the aromatic protons are closely spaced, making a definitive interpretation challenging. In the 13C-NMR spectrum, the identification of the four most shifted quaternary carbons as doublets can be certainly attributed to C-F interactions, while the four most intense signals correspond to tertiary aromatic C-H bonds within the carbazole ring. Beyond these attributions, attempting further peak assignments seems unwarranted, except to mention that the number of signals aligns with the carbon count in the molecule.

It is essential to address the potential influence of solvent impurities and the challenging proton count in our molecule when interpreting the spectra.

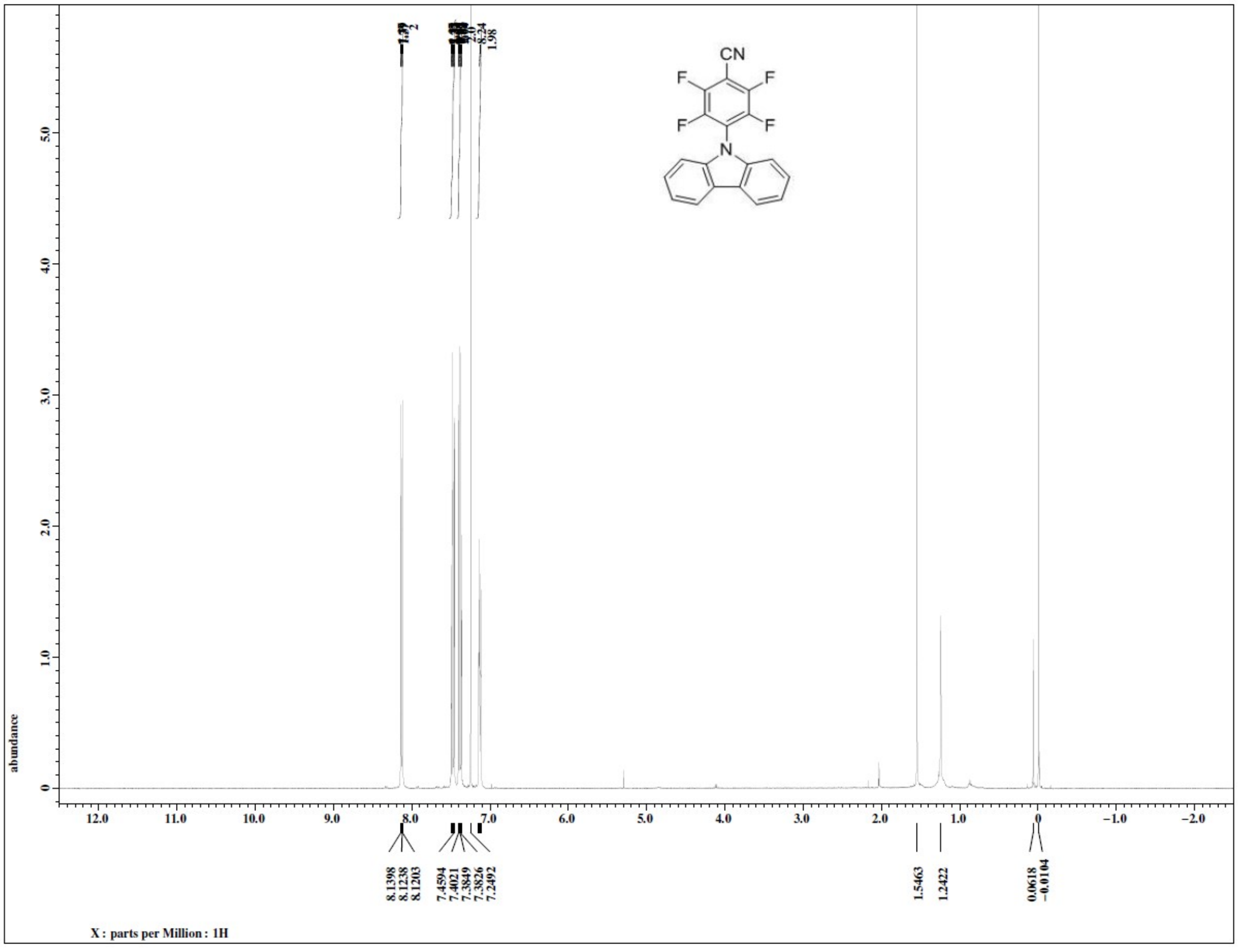

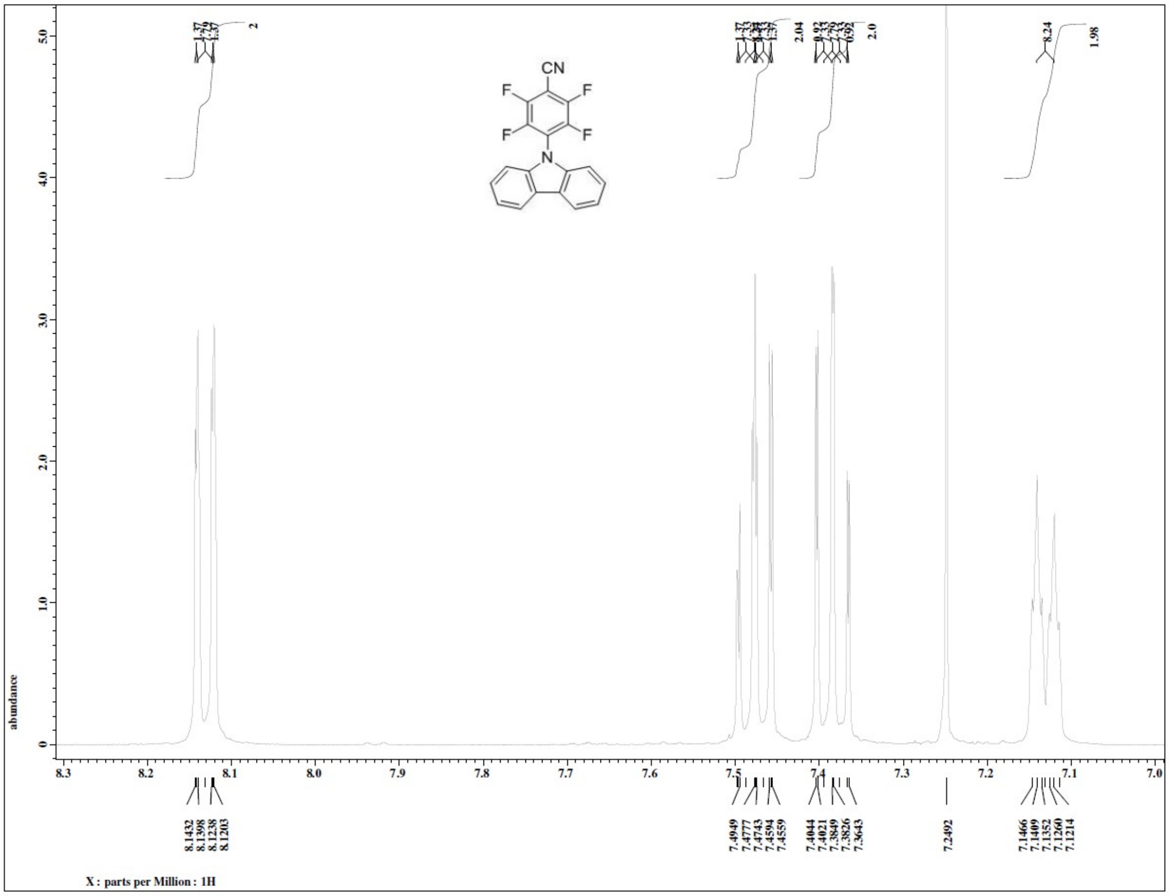CN
F
F
F
F
N
abundance
5.0
4.0
3.0
2.0
1.0
0
2
2.04
2.0
8.24
1.98
8.3
8.2
8.1
8.0
7.9
7.8
7.7
7.6
7.5
7.4
7.3
7.2
7.1
7.0
8.1432
8.1398
8.1238
8.1203
7.4949
7.4777
7.4743
7.4594
7.4559
7.4044
7.4021
7.3849
7.3826
7.3643
7.2492
7.1466
7.1409
7.1352
7.1260
7.1214
X : parts per Million : 1H

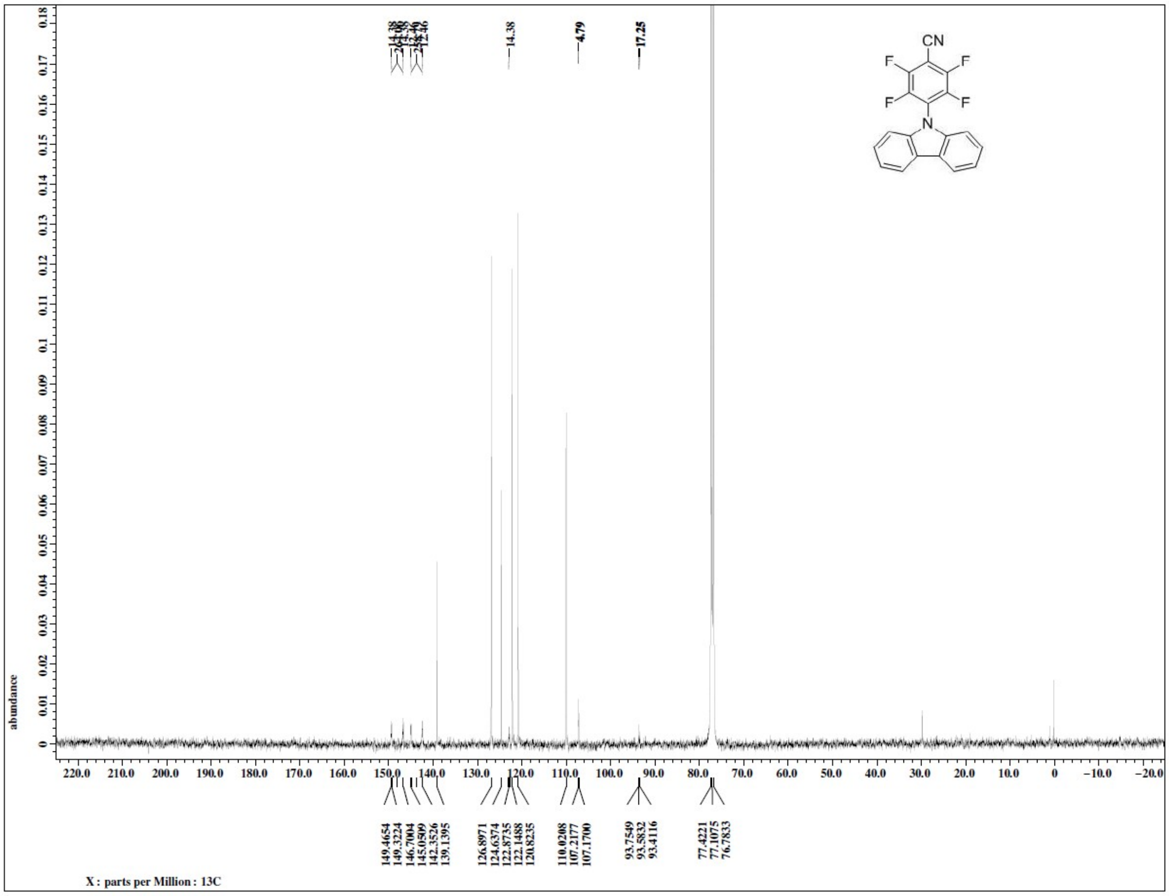
CN
F
F
F
F
N
abundance
0.18
0.17
0.16
0.15
0.14
0.13
0.12
0.11
0.1
0.09
0.08
0.07
0.06
0.05
0.04
0.03
0.02
0.01
0
14.38
4.79
17.25
220.0
210.0
200.0
190.0
180.0
170.0
160.0
150.0
140.0
130.0
120.0
110.0
100.0
90.0
80.0
70.0
60.0
50.0
40.0
30.0
20.0
10.0
0
−10.0
−20.0
149.4654
149.3224
146.7004
145.0509
142.3526
139.1395
126.8971
124.6374
122.8735
122.1488
120.8235
110.0208
107.2177
107.1700
93.7549
93.5832
93.4116
77.4221
77.1075
76.7833
X : parts per Million : 13C

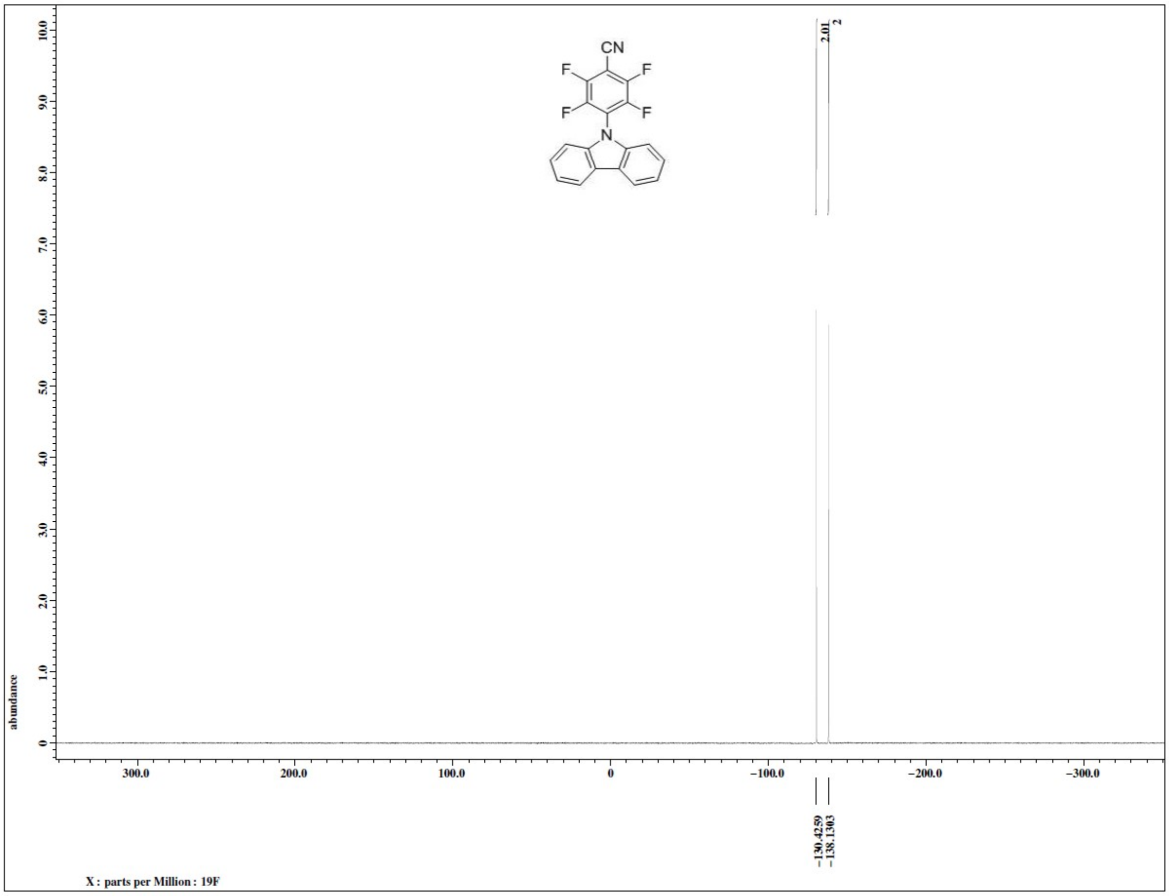

Monoisotopic Mass, Odd Electron Ions
177 formula(e) evaluated with 1 results within limits (all results (up to 1000) for each mass)
Elements Used:
C: 0-100   H: 0-110   N: 0-5   O: 0-10   F: 4-4
PPSM_Yang-N1 21 (0.571) Cm (18:24)
1: TOF MS ES+

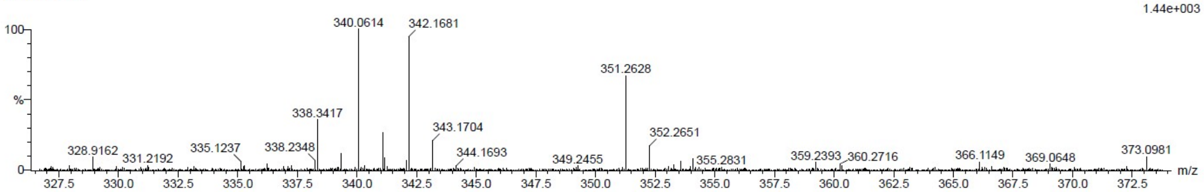

```
Minimum:                                  -1.5
Maximum:                  5.0      5.0    50.0

Mass       Calc. Mass     mDa      PPM     DBE      i-FIT     i-FIT (Norm) Formula

340.0614   340.0624       -1.0     -2.9    15.0     648.3     0.0          C19  H8  N2  F4
```

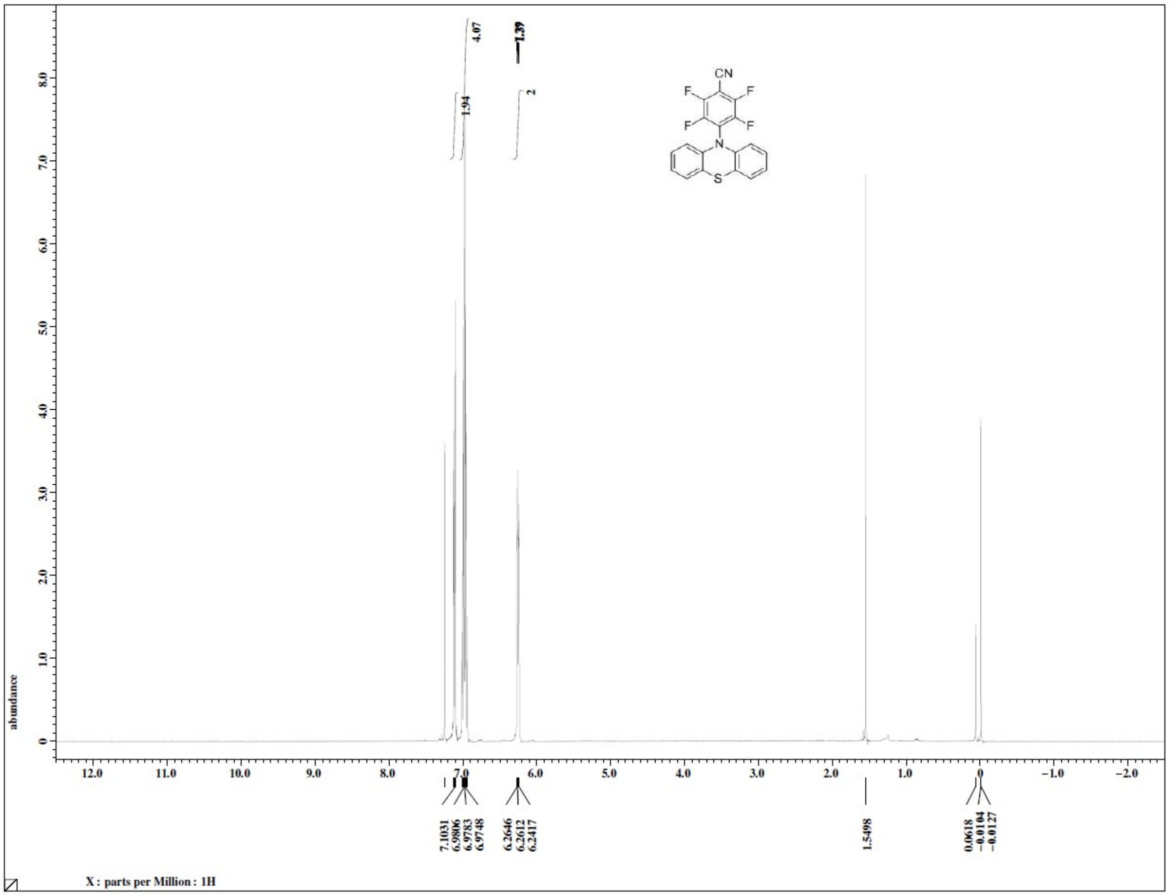

CN
F
F
F
F
N
S
4.07
1.39
1.94
2
8.0
7.0
6.0
5.0
4.0
3.0
2.0
1.0
0
abundance
12.0
11.0
10.0
9.0
8.0
7.0
6.0
5.0
4.0
3.0
2.0
1.0
0
−1.0
−2.0
7.1031
6.9806
6.9783
6.9748
6.2646
6.2612
6.2417
1.5498
0.0618
−0.0104
−0.0127
X : parts per Million : 1H

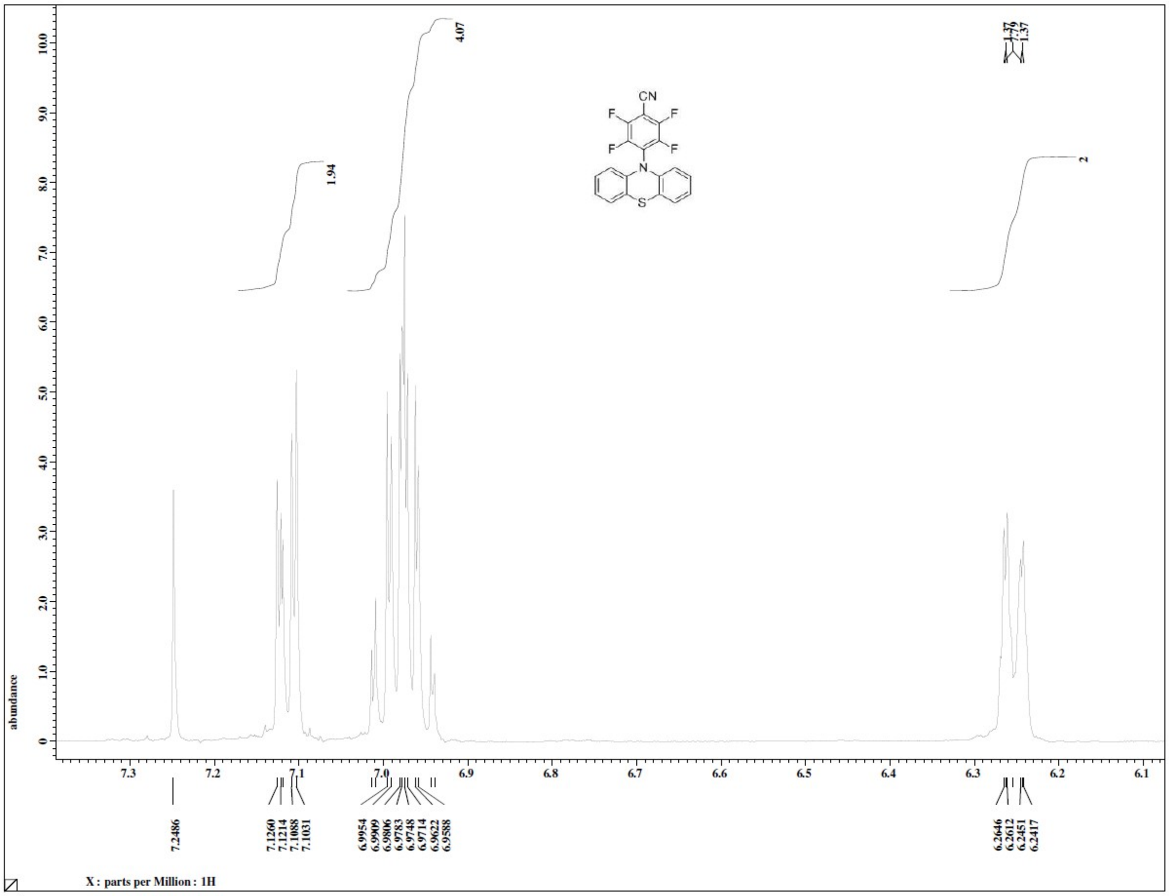
abundance
10.0
9.0
8.0
7.0
6.0
5.0
4.0
3.0
2.0
1.0
0
1.94
4.07
1.37
1.37
2
CN
F
F
F
F
N
S
7.3
7.2
7.1
7.0
6.9
6.8
6.7
6.6
6.5
6.4
6.3
6.2
6.1
7.2486
7.1260
7.1214
7.1088
7.1031
6.9954
6.9909
6.9806
6.9783
6.9748
6.9714
6.9622
6.9588
6.2646
6.2612
6.2451
6.2417
X : parts per Million : 1H

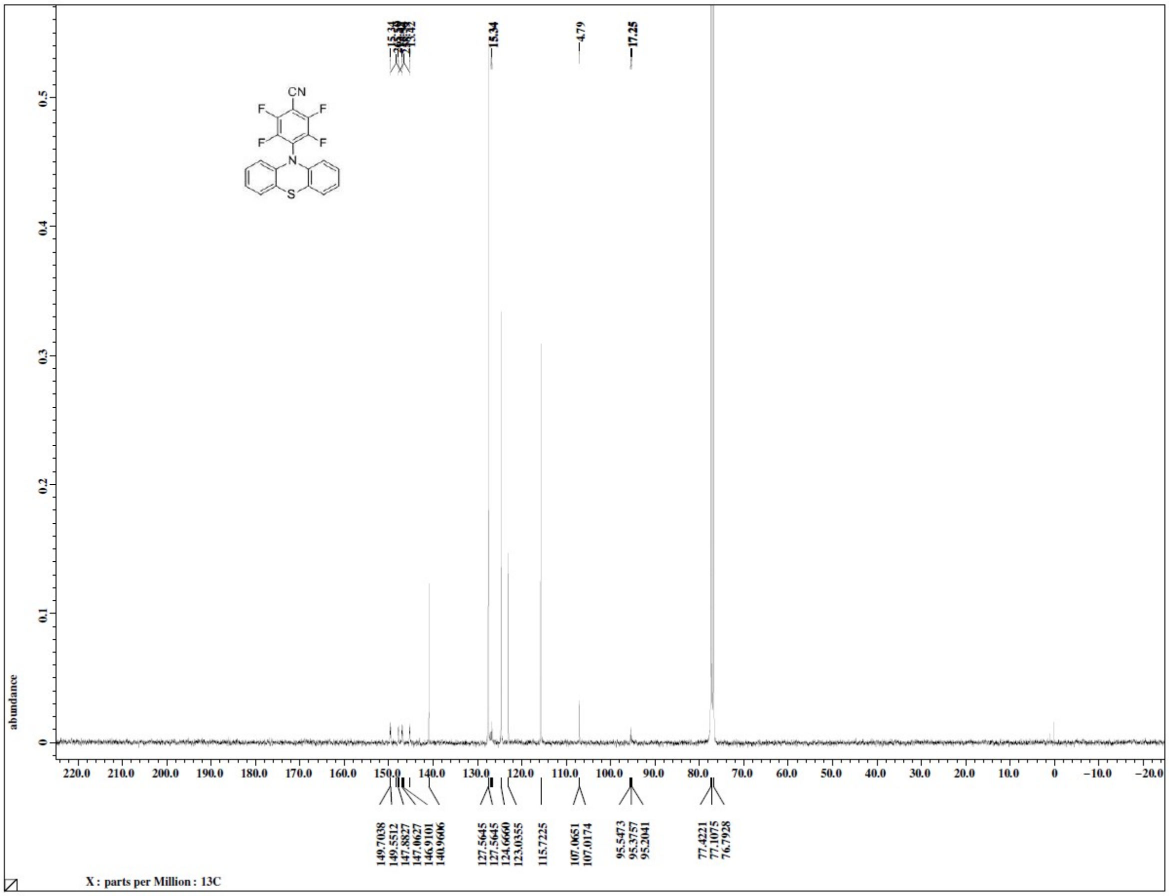
15.34
13.42
15.34
4.79
17.25
CN
F
F
F
F
N
S
abundance
0.5
0.4
0.3
0.2
0.1
0
220.0
210.0
200.0
190.0
180.0
170.0
160.0
150.0
140.0
130.0
120.0
110.0
100.0
90.0
80.0
70.0
60.0
50.0
40.0
30.0
20.0
10.0
0
−10.0
−20.0
149.7038
149.5512
147.8827
147.0627
146.9101
140.9606
127.5645
127.5645
124.6660
123.0355
115.7225
107.0651
107.0174
95.5473
95.3757
95.2041
77.4221
77.1075
76.7928
X : parts per Million : 13C

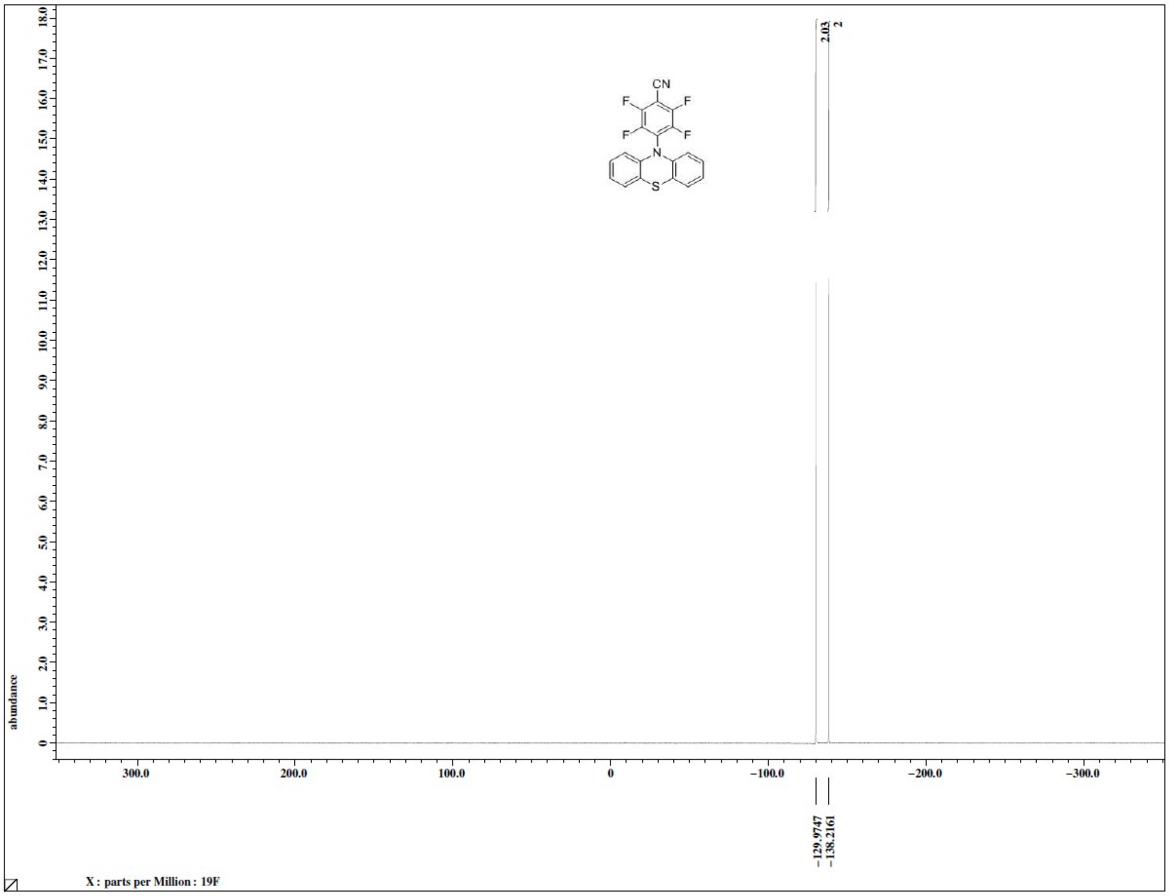

Monoisotopic Mass, Odd Electron Ions
288 formula(e) evaluated with 3 results within limits (all results (up to 1000) for each mass)
Elements Used:
C: 0-100 H: 0-110 N: 0-10 O: 0-10 F: 4-4 S: 1-1
PPSM_Yang-N16 22 (0.590) Cm (19:25)
1: TOF MS ES+

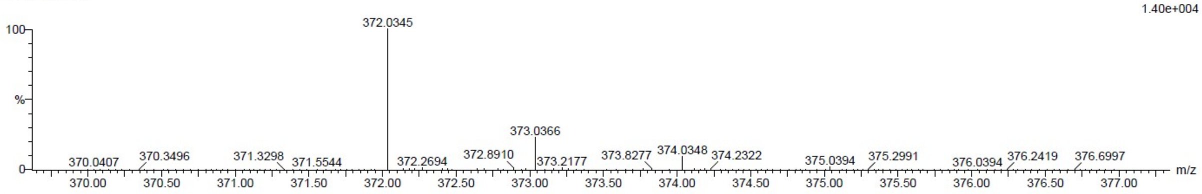

```
Minimum:                                 -1.5
Maximum:              5.0      5.0      100.0

Mass      Calc. Mass  mDa      PPM      DBE      i-FIT     i-FIT (Norm) Formula

372.0345  372.0344    0.1      0.3      15.0     500.4     0.0          C19  H8  N2  F4  S
          372.0363    -1.8     -4.8     2.0      512.2     11.9         C7  H12  N4  O7  F4  S
          372.0336    0.9      2.4      3.0      514.7     14.4         C3  H8  N10  O5  F4  S
```

3.8 OPTIMIZED GEOMETRIES OF THE CALCULATED STRUCTURES

Data for **Phx-BzN** can be found in the SI of *J. Phys. Chem. B* **2022,** *126* (14), 2740-2753.

***Cz-BzN** ground state (S_0) geometry*

Symbol	X	Y	Z
C	1.337801	-0.846345	-0.850521
C	2.726998	-0.854784	-0.842941
C	3.454065	-0.000002	-0.000003
C	2.727005	0.854781	0.842939
C	1.337808	0.846345	0.850526
C	0.605406	0.000001	0.000005
C	4.880903	-0.000004	-0.000008
N	6.043529	-0.000005	-0.000011
F	3.377859	1.675252	1.675007
F	0.692199	1.651983	1.704083
F	0.692186	-1.651983	-1.704073
F	3.377846	-1.675256	-1.675013
N	-0.793095	0.000003	0.00001
C	-1.616138	-1.109223	0.280507
C	-1.616136	1.109227	-0.280498
C	-1.25793	-2.407411	0.644714
C	-2.967949	-0.702937	0.180381
C	-1.257927	2.407416	-0.6447
C	-2.967948	0.702939	-0.180386
C	-2.28838	-3.314903	0.895901
H	-0.219421	-2.711996	0.7314
C	-3.984002	-1.631071	0.438941
C	-2.288375	3.314906	-0.895898

H	-0.219417	2.712002	-0.731375
C	-3.984	1.631072	-0.438954
C	-3.63787	-2.934443	0.79252
H	-2.038427	-4.334186	1.177219
H	-5.028325	-1.337905	0.369847
C	-3.637866	2.934444	-0.79253
H	-2.03842	4.33419	-1.177212
H	-5.028322	1.337905	-0.36987
H	-4.417153	-3.663907	0.994472
H	-4.417148	3.663907	-0.994489

***Cz-BzN** 1st singlet excited state (S_1) geometry*

Symbol	X	Y	Z
C	-1.243744	-0.595876	-1.210859
C	-2.586561	-0.368233	-1.208361
C	-3.321513	-0.200818	0.000037
C	-2.586543	-0.368216	1.208425
C	-1.243727	-0.595862	1.210896
C	-0.496607	-0.742846	0.000013
C	-4.696031	0.118374	0.000063
N	-5.831015	0.374332	-0.00019
F	-3.252192	-0.345783	2.370421
F	-0.581313	-0.762173	2.377064
F	-0.58135	-0.762193	-2.377037
F	-3.252234	-0.345799	-2.370345
N	0.839755	-0.214128	0.000001
C	1.178088	1.128911	-0.000002
C	1.983151	-0.966751	-0.000007
C	0.311572	2.222814	0.000007

C	2.588502	1.259149	-0.000015
C	2.084918	-2.363607	-0.000004
C	3.118004	-0.108395	-0.000018
C	0.901626	3.489011	0.000002
H	-0.763551	2.086778	0.000017
C	3.15075	2.517801	-0.00002
C	3.370621	-2.899756	-0.000014
H	1.1919	-2.976249	0.000005
C	4.378835	-0.661322	-0.000027
C	2.288741	3.635101	-0.000011
H	0.270022	4.369808	0.000008
H	4.226943	2.657529	-0.00003
C	4.494175	-2.068813	-0.000025
H	3.501376	-3.975665	-0.000012
H	5.268974	-0.040931	-0.000036
H	2.718163	4.631146	-0.000015
H	5.48326	-2.514311	-0.000032

Cz-BzN *1st triplet excited state (T_1) geometry*

X	Y	Z
1.385371	0.552223	1.149062
2.695841	0.654832	0.849986
3.311934	-0.200893	-0.14623
2.51915	-1.286811	-0.647335
1.217414	-1.431036	-0.30566
0.520687	-0.440197	0.527193
4.620423	0.026734	-0.596131
5.716371	0.206519	-0.951928
3.12208	-2.206493	-1.405033

0.530595	-2.483152	-0.761363
0.846252	1.314498	2.110275
3.484728	1.505714	1.509176
-0.783452	-0.090952	0.212119
-1.251007	1.1848	-0.167912
-1.885282	-0.966216	0.249453
-0.526678	2.354083	-0.393686
-2.642791	1.116343	-0.37934
-1.92596	-2.293068	0.670958
-3.047945	-0.258316	-0.111671
-1.242274	3.479539	-0.796593
0.548607	2.398552	-0.272624
-3.33716	2.246577	-0.791006
-3.167213	-2.924475	0.665261
-1.032109	-2.812606	0.992827
-4.278665	-0.902885	-0.104958
-2.62732	3.432085	-0.988872
-0.708676	4.407391	-0.971404
-4.407953	2.206975	-0.964006
-4.327197	-2.245421	0.27389
-3.23371	-3.960875	0.977993
-5.185419	-0.370639	-0.37439
-3.153088	4.325554	-1.308147
-5.278955	-2.765831	0.282456

Pht-BzN *ground state (S_0) geometry*

Symbol	X	Y	Z

C	1.356839	-0.00059	1.241516
C	2.743995	-0.000606	1.346666
C	3.55453	0.000067	0.201405
C	2.922244	0.000763	-1.050985
C	1.535416	0.000795	-1.149196
C	0.719312	0.000125	-0.008431
C	4.978677	0.00001	0.306512
N	6.137961	-0.00004	0.390535
F	3.659678	0.001369	-2.167601
F	0.975557	0.001373	-2.367627
F	0.626636	-0.001269	2.359924
F	3.310839	-0.00132	2.557734
N	-0.694378	0.000084	-0.076237
C	-1.379485	1.244551	-0.206636
C	-1.379286	-1.244444	-0.207216
C	-2.70722	1.356694	0.243952
C	-0.762103	2.368755	-0.771914
C	-2.70697	-1.357077	0.243384
C	-0.761735	-2.368211	-0.773189
C	-3.400284	2.561932	0.099915
S	-3.482263	-0.000445	1.097374
C	-1.446005	3.582349	-0.872375
H	0.257612	2.306113	-1.135755
C	-3.399787	-2.562392	0.098797
H	0.257917	-2.305137	-1.137137
C	-1.445388	-3.581897	-0.874222
C	-2.769588	3.682848	-0.4433
H	-4.432168	2.620462	0.435633
H	-0.940556	4.442197	-1.302989
H	-4.431635	-2.621313	0.434557

C	-2.768899	-3.682897	-0.44504
H	-0.939818	-4.44141	-1.305361
H	-3.310537	4.620464	-0.532292
H	-3.309657	-4.620583	-0.534452

Pht-BzN *1st singlet excited state (S_1) geometry*

Symbol	X	Y	Z
C	1.359282	-0.605912	-1.211059
C	2.714084	-0.461759	-1.210878
C	3.455359	-0.317438	0.000019
C	2.714076	-0.461483	1.210945
C	1.359273	-0.60564	1.21115
C	0.611834	-0.654287	0.000049
C	4.84062	-0.054485	-0.000006
N	5.986362	0.152051	-0.00002
F	3.384876	-0.509703	2.370388
F	0.685353	-0.757848	2.374407
F	0.685368	-0.758386	-2.374286
F	3.384892	-0.510241	-2.370306
N	-0.734426	-0.128005	-0.000006
C	-1.775177	-1.045093	0.000029
C	-0.906404	1.251959	-0.000082
C	-3.140299	-0.662781	0.000032
C	-1.481799	-2.430905	0.000064
C	-2.182138	1.870638	-0.00008
C	0.231149	2.097057	-0.000142
C	-4.154892	-1.632399	0.000069
S	-3.669907	0.984868	0.000006
C	-2.48982	-3.367759	0.0001

H	-0.445224	-2.734304	0.000063
C	-2.303849	3.268222	-0.000138
H	1.220515	1.665268	-0.000146
C	0.092361	3.467299	-0.0002
C	-3.839003	-2.975145	0.000102
H	-5.191419	-1.308695	0.00007
H	-2.23172	-4.420893	0.000126
H	-3.295642	3.710847	-0.000135
C	-1.178283	4.065765	-0.000199
H	0.983481	4.084583	-0.000246
H	-4.629178	-3.717843	0.00013
H	-1.278484	5.145313	-0.000243

***Pht-BzN** 1st triplet excited state (T_1) geometry*

Symbol	X	Y	Z
C	1.365908	-1.131345	-0.869307
C	2.72053	-0.993793	-0.927843
C	3.452676	-0.323207	0.094541
C	2.699889	0.108736	1.227216
C	1.34515	-0.015877	1.2785
C	0.600985	-0.634523	0.229906
C	4.842254	-0.102689	-0.00611
N	5.99036	0.070905	-0.084796
F	3.360392	0.606076	2.280594
F	0.662686	0.399352	2.367153
F	0.707254	-1.786054	-1.853357
F	3.39686	-1.544989	-1.943654
N	-0.736521	-0.14597	-0.01616
C	-1.787276	-1.049728	0.087287

C	-0.904776	1.202589	-0.313708
C	-3.141327	-0.638543	0.121783
C	-1.512001	-2.434311	0.178979
C	-2.159512	1.857096	-0.232757
C	0.221622	1.977948	-0.687159
C	-4.170977	-1.586326	0.227813
S	-3.632202	1.025282	0.14535
C	-2.535671	-3.351092	0.273702
H	-0.483342	-2.761974	0.166502
C	-2.261542	3.237463	-0.456266
H	1.181783	1.498391	-0.811289
C	0.100314	3.330708	-0.915084
C	-3.876167	-2.932728	0.298335
H	-5.200861	-1.243724	0.254332
H	-2.295603	-4.406831	0.329938
H	-3.234123	3.714094	-0.379628
C	-1.141366	3.974959	-0.784502
H	0.978228	3.896892	-1.204741
H	-4.677477	-3.659	0.375891
H	-1.22727	5.041621	-0.958474

4 REFERENCES

1. Castillo-Peinado, L. d. l. S.; Luque de Castro, M. D., The role of ultrasound in pharmaceutical production: sonocrystallization. *Journal of Pharmacy and Pharmacology* **2016,** *68* (10), 1249-1267.
2. Ruecroft, G.; Hipkiss, D.; Ly, T.; Maxted, N.; Cains, P. W., Sonocrystallization: The use of ultrasound for improved industrial crystallization. *Organic Process Research & Development* **2005,** *9* (6), 923-932.
3. L, K., Ultrasound. Its Chemical, Physical, and Biological Effects. Kenneth S. Suslick, Ed. VCH, New York, 1988 xiv, 336 pp., illus. $65. *Science (New York, N.Y.)* **1989,** *243* (4897), 1499.
4. Kenneth S. Suslick, E. V., Ultrasound. Its Chemical, Physical, and Biological Effects. *Science* **17 Mar 1989,** *243* (4897).
5. Leighton, T., The Acoustic Bubble, 1st Edition. *Academic Press* **15th May 1997**, 613.
6. Sander, J. R. G.; Zeiger, B. W.; Suslick, K. S., Sonocrystallization and sonofragmentation. *Ultrasonics Sonochemistry* **2014,** *21* (6), 1908-1915.
7. Kim, H. N.; Suslick, K. S., The Effects of Ultrasound on Crystals: Sonocrystallization and Sonofragmentation. *Crystals* **2018,** *8* (7).
8. Würth, C.; Grabolle, M.; Pauli, J.; Spieles, M.; Resch-Genger, U., Relative and absolute determination of fluorescence quantum yields of transparent samples. *Nature protocols* **2013,** *8* (8), 1535-50.
9. Dias, F. B.; Penfold, T. J.; Monkman, A. P., Photophysics of thermally activated delayed fluorescence molecules. *Methods and Applications in Fluorescence* **2017,** *5* (1).
10. Dias, F. B.; Santos, J.; Graves, D. R.; Data, P.; Nobuyasu, R. S.; Fox, M. A.; Batsanov, A. S.; Palmeira, T.; Berberan-Santos, M. N.; Bryce, M. R.; Monkman, A. P., The Role of Local Triplet Excited States and D-A Relative Orientation in Thermally Activated Delayed Fluorescence: Photophysics and Devices. *Adv Sci (Weinh)* **2016,** *3* (12), 1600080.
11. Maggiore, A.; Qu, Y. Y.; Guillot, R.; Pander, P.; Vasylieva, M.; Data, P.; Dias, F. B.; Audebert, P.; Clavier, G.; Miomandre, F., Novel Easy to Synthesize Benzonitrile Compounds with Mixed Carbazole and Phenoxazine Substituents Exhibiting Dual Emission and TADF Properties. *Journal of Physical Chemistry B* **2022,** *126* (14), 2740-2753.
12. Sheldrick, G. M. S.-. Program for Crystal Structure Solution. **1997**.
13. Sheldrick, G. M., A short history of SHELX. *Acta Crystallographica Section A: Foundations of Crystallography* **2008,** *64* (1), 112-122.
14. Farrugia, L. J., WinGX suite for small-molecule single-crystal crystallography. *journal of Applied Crystallography* **1999,** *32* (4), 837-838.
15. Altamura, D.; Lassandro, R.; Vittoria, F.; De Caro, L.; Siliqi, D.; Ladisa, M.; Giannini, C., X-ray microimaging laboratory (XMI-LAB). *Journal of Applied Crystallography* **2012,** *45* (4), 869-873.
16. Siliqi, D.; De Caro, L.; Ladisa, M.; Scattarella, F.; Mazzone, A.; Altamura, D.; Sibillano, T.; Giannini, C., SUNBIM: a package for X-ray imaging of nano- and biomaterials using SAXS, WAXS, GISAXS and GIWAXS techniques. *Journal of Applied Crystallography* **2016,** *49* (3), 1107-1114.
17. Speck, F.; Rombach, D.; Wagenknecht, H. A., N-Arylphenothiazines as strong donors for photoredox catalysis - pushing the frontiers of nucleophilic addition of alcohols to alkenes. *Beilstein Journal of Organic Chemistry* **2019,** *15*, 52-59.
18. McCarthy, B. G.; Pearson, R. M.; Lim, C. H.; Sartor, S. M.; Damrauer, N. H.; Miyake, G. M., Structure-Property Relationships for Tailoring Phenoxazines as Reducing Photoredox Catalysts. *Journal of the American Chemical Society* **2018,** *140* (15), 5088-5101.
19. Tanaka, H.; Shizu, K.; Nakanotani, H.; Adachi, C., Dual Intramolecular Charge-Transfer Fluorescence Derived from a Phenothiazine-Triphenyltriazine Derivative. *Journal of Physical Chemistry C* **2014,** *118* (29), 15985-15994.

20. Gaussian 16, R. B., M. J. Frisch, G. W. Trucks, H. B. Schlegel, G. E. Scuseria, M. A. Robb, J. R. Cheeseman, G. Scalmani, V. Barone, G. A. Petersson, H. Nakatsuji, X. Li, M. Caricato, A. V. Marenich, J. Bloino, B. G. Janesko, R. Gomperts, B. Mennucci, H. P. Hratchian, J. V. Ortiz, A. F. Izmaylov, J. L. Sonnenberg, D. Williams-Young, F. Ding, F. Lipparini, F. Egidi, J. Goings, B. Peng, A. Petrone, T. Henderson, D. Ranasinghe, V. G. Zakrzewski, J. Gao, N. Rega, G. Zheng, W. Liang, M. Hada, M. Ehara, K. Toyota, R. Fukuda, J. Hasegawa, M. Ishida, T. Nakajima, Y. Honda, O. Kitao, H. Nakai, T. Vreven, K. Throssell, J. A. Montgomery, Jr., J. E. Peralta, F. Ogliaro, M. J. Bearpark, J. J. Heyd, E. N. Brothers, K. N. Kudin, V. N. Staroverov, T. A. Keith, R. Kobayashi, J. Normand, K. Raghavachari, A. P. Rendell, J. C. Burant, S. S. Iyengar, J. Tomasi, M. Cossi, J. M. Millam, M. Klene, C. Adamo, R. Cammi, J. W. Ochterski, R. L. Martin, K. Morokuma, O. Farkas, J. B. Foresman, and D. J. Fox, Gaussian, Inc., Wallingford CT., **2016**.
21. N. M. O'Boyle, A. L. T. a. K. M. L., *J. Comp. Chem* **2008,** *29*, 839–845.